EUROPEAN ORGANIZATION FOR NUCLEAR RESEARCH (CERN)

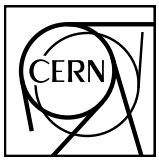

CERN-EP-2021-138
12 July 2021

Angular analysis of the rare decay $B_s^0 \to \phi\mu^+\mu^-$

LHCb collaboration[†]

Abstract

An angular analysis of the rare decay $B_s^0 \to \phi\mu^+\mu^-$ is presented, using proton-proton collision data collected by the LHCb experiment at centre-of-mass energies of 7, 8 and 13 TeV, corresponding to an integrated luminosity of 8.4 fb^{-1}. The observables describing the angular distributions of the decay $B_s^0 \to \phi\mu^+\mu^-$ are determined in regions of q^2, the square of the dimuon invariant mass. The results are consistent with Standard Model predictions.

Submitted to JHEP

[†]Authors are listed at the end of this paper.

1 Introduction

Transitions of a b quark to an s quark and a pair of oppositely charged leptons are forbidden at tree level in the Standard Model (SM) and only proceed via higher-order electroweak (loop) diagrams. These transitions constitute powerful probes for New Physics (NP) contributions beyond the SM that can appear in competing diagrams and significantly affect branching fractions and angular distributions of $b \to s\ell^+\ell^-$ decays. Recent studies of $b \to s\ell^+\ell^-$ decays have observed tensions with SM predictions in measurements of branching fractions [1–6], angular observables [7–13] and tests of lepton universality [13–21]. One of the most significant deviations from SM expectations is observed in the determination of the branching fraction of $B^0_s \to \phi\mu^+\mu^-$ decays [6].[1] The measured branching fraction is found to be 3.6 standard deviations (σ) below a precise SM prediction [22–26] in the squared dimuon mass (q^2) region $1.1 < q^2 < 6.0\,\text{GeV}^2/c^4$. Angular analyses of $b \to s\ell^+\ell^-$ decays provide information complementary to branching fraction measurements, allowing to probe the operator structure of potential NP contributions. An angular analysis of the decay $B^0_s \to \phi\mu^+\mu^-$ [4], using proton-proton (pp) collision data corresponding to $3\,\text{fb}^{-1}$ recorded by the LHCb experiment during 2011–2012, found the angular distributions to be compatible with SM predictions.

This paper presents an updated angular analysis of $B^0_s \to \phi\mu^+\mu^-$ decays, where the ϕ meson is reconstructed in the K^+K^- final state, using pp collisions recorded by the LHCb experiment corresponding to a total integrated luminosity of $8.4\,\text{fb}^{-1}$. The data were collected at centre-of-mass energies of 7 TeV (2011), 8 TeV (2012) and 13 TeV (2016–2018) during the LHC Run 1 and Run 2, respectively. For the purposes of this analysis, the data are split according to the 2011–2012 ($3\,\text{fb}^{-1}$), 2016 ($1.7\,\text{fb}^{-1}$) and 2017–2018 ($3.7\,\text{fb}^{-1}$) data-taking periods. The higher $b\bar{b}$ production cross-section in Run 2 [27, 28] yields an approximate four-fold increase in the total number of produced B^0_s mesons compared to the Run 1 data. The criteria used to select candidates in this analysis are identical to those of Ref. [6], with an adapted q^2 binning scheme.

Neglecting the natural width of the ϕ meson, the $B^0_s \to \phi(\to K^+K^-)\mu^+\mu^-$ decay rate depends on q^2, three decay angles, θ_l, θ_K, and ϕ, and the decay time of the B^0_s meson [29]. The angle θ_l (θ_K) is defined as the angle of the μ^- (K^-) with respect to the direction of flight of the B^0_s meson in the $\mu^+\mu^-$ (K^+K^-) centre-of-mass frame, and ϕ as the angle between the $\mu^+\mu^-$ and the K^+K^- planes in the B^0_s meson centre-of-mass frame. As the decay flavour of the B^0_s meson cannot be determined from the flavour-symmetric final state, the same angular definition is used for both B^0_s and $\overline{B}^0_s$ decays.

The untagged CP-averaged angular decay rate, $\Gamma + \overline{\Gamma}$, is measured integrated over the B^0_s decay time and is given for a specific q^2 region by

$$\begin{aligned}\frac{1}{\mathrm{d}(\Gamma+\overline{\Gamma})/\mathrm{d}q^2}\frac{\mathrm{d}^3(\Gamma+\overline{\Gamma})}{\mathrm{d}\cos\theta_l\,\mathrm{d}\cos\theta_K\,\mathrm{d}\phi} = \frac{9}{32\pi}\Big[&\tfrac{3}{4}(1-F_\mathrm{L})\sin^2\theta_K(1+\tfrac{1}{3}\cos 2\theta_l)\\ &+ F_\mathrm{L}\cos^2\theta_K(1-\cos 2\theta_l) + S_3\sin^2\theta_K\sin^2\theta_l\cos 2\phi\\ &+ S_4\sin 2\theta_K\sin 2\theta_l\cos\phi + A_5\sin 2\theta_K\sin\theta_l\cos\phi\\ &+ \tfrac{4}{3}A^{CP}_\mathrm{FB}\sin^2\theta_K\cos\theta_l + S_7\sin 2\theta_K\sin\theta_l\sin\phi\\ &+ A_8\sin 2\theta_K\sin 2\theta_l\sin\phi + A_9\sin^2\theta_K\sin^2\theta_l\sin 2\phi\Big], \qquad (1)\end{aligned}$$

[1] The inclusion of the charge-conjugated mode is implied throughout this paper unless otherwise stated, and the shorthand ϕ refers to the $\phi(1020)$ meson in the following.

where the angular observables $F_{\rm L}$ and $S_{3,4,7}$ are *CP* averages, and $A_{\rm FB}^{CP}$ and $A_{5,8,9}$ are *CP* asymmetries [30, 31]. The presence of *CP* asymmetries in Eq. 1 is due to the need to use identical angular definitions for the B_s^0 and $\overline{B}_s^0$ modes [29, 31]. Of particular interest are the T-odd *CP* asymmetries A_8 and A_9, which are predicted to be close to zero in the SM, but can be large in the presence of NP contributions [31]. As the decay flavour of the B_s^0 meson is unknown, the *CP*-averaged observable S_5 (P_5'), which has received a lot of attention in the study of $B^0 \to K^{*0}\mu^+\mu^-$ decays [8], cannot be accessed by this analysis.

2 Detector and simulation

The LHCb detector [32, 33] is a single-arm forward spectrometer covering the pseudorapidity range $2 < \eta < 5$, designed for the study of particles containing b or c quarks. The detector includes a high-precision tracking system consisting of a silicon-strip vertex detector surrounding the pp interaction region [34], a large-area silicon-strip detector located upstream of a dipole magnet with a bending power of about 4 Tm, and three stations of silicon-strip detectors and straw drift tubes [35, 36] placed downstream of the magnet. The tracking system provides a measurement of the momentum, p, of charged particles with a relative uncertainty that varies from 0.5% at low momentum to 1.0% at 200 GeV/c. The minimum distance of a track to a primary pp collision vertex (PV), the impact parameter (IP), is measured with a resolution of $(15 + 29/p_{\rm T})\,\mu$m, where $p_{\rm T}$ is the component of the momentum transverse to the beam, in GeV/c. Different types of charged hadrons are distinguished using information from two ring-imaging Cherenkov detectors [37]. Muons are identified by a system composed of alternating layers of iron and multiwire proportional chambers [38].

The online event selection is performed by a trigger system [39]. In this analysis, an initial hardware stage uses information from the muon system to require at least one muon with significant $p_{\rm T}$ in the event. Events passing the hardware trigger enter the software trigger, where a full event reconstruction is applied. At this stage, further requirements are placed on the kinematics of the muon candidates and on the topology of the signal candidate.

Simulated samples are used to determine the effect of reconstruction and selection on the angular distributions of the signal candidates, as well as to estimate expected signal yields and contamination from specific background processes. The pp collisions are simulated using Pythia [40] with a specific LHCb configuration [41]. Decays of unstable particles are described by EvtGen [42], in which final-state radiation is generated using Photos [43]. The interaction of the generated particles with the detector, and its response, are implemented using the Geant4 toolkit [44] as described in Ref. [45]. Residual mismodelling of the particle identification performance, the $p_{\rm T}$ spectrum of the B_s^0 mesons, the track multiplicity and the efficiency of the hardware trigger is corrected using high-yield control samples from data.

3 Selection of signal candidates

All tracks in the $K^+K^-\mu^+\mu^-$ final-state are required to have significant $\chi^2_{\rm IP}$ with respect to any PV, where $\chi^2_{\rm IP}$ is defined as the difference in the vertex-fit χ^2 of a given PV

reconstructed with and without the track being considered. The final-state particles are further required to be well identified using particle identification information.

The B_s^0 decay vertex, determined by fitting the four final-state tracks, is required to be of good quality and to be significantly displaced from any PV in the event. The angle between the vector connecting the associated PV with the B_s^0 decay vertex and the momentum of the B_s^0 candidate ($\theta_{\rm DIRA}$) is required to be small. The associated PV is defined as that which fits best to the flight direction of the B_s^0 candidate.

Candidates are accepted if the invariant reconstructed $K^+K^-\mu^+\mu^-$ mass is in the range $5270 < m(K^+K^-\mu^+\mu^-) < 5700\,{\rm MeV}/c^2$ and the invariant mass of the K^+K^- system is within $12\,{\rm MeV}/c^2$ of the known ϕ mass [46]. Candidates are further required to have a q^2 value in the range $0.1 < q^2 < 18.9\,{\rm GeV}^2/c^4$.

The resonant $B_s^0 \to \phi(\to \mu^+\mu^-)\phi$, $B_s^0 \to J/\psi(\to \mu^+\mu^-)\phi$ and $B_s^0 \to \psi(2S)(\to \mu^+\mu^-)\phi$ decays dominate the experimental q^2 spectrum in the q^2 regions of $0.98 < q^2 < 1.1\,{\rm GeV}^2/c^4$, $8 < q^2 < 11\,{\rm GeV}^2/c^4$ and $12.5 < q^2 < 15\,{\rm GeV}^2/c^4$, respectively. These q^2 regions are therefore excluded from the signal selection but $B_s^0 \to J/\psi\phi$ candidates in the $8 < q^2 < 11\,{\rm GeV}^2/c^4$ region are retained as a control mode to develop selection criteria, validate fit behaviour and derive corrections to the simulation.

Background originating from a random combination of tracks (combinatorial background) is reduced using a boosted decision tree (BDT) [47] classifier trained with the AdaBoost algorithm [48] as implemented in the TMVA package [49]. The BDT classifier is trained on data and its performance verified using standard cross-validation techniques [50]. The upper mass sideband, defined as $m(K^+K^-\mu^+\mu^-) > 5567\,{\rm MeV}/c^2$, is used as a proxy for the combinatorial background and enriched in background by relaxing the requirement on the invariant mass of the K^+K^- system from $12\,{\rm MeV}/c^2$ to $50\,{\rm MeV}/c^2$ around the known ϕ mass. As a signal proxy, a sample of $B_s^0 \to J/\psi\phi$ candidates from data in a $50\,{\rm MeV}/c^2$ mass range around the known B_s^0 mass [46] is used, for which background contributions have been statistically subtracted [51].

The classifier combines the transverse momentum of the B_s^0, the angle $\theta_{\rm DIRA}$, the fit quality of the B_s^0 vertex (vertex-fit χ^2), its displacement from the associated PV and the $\chi^2_{\rm IP}$ and particle identification information of all final-state tracks. The selection criterion on the BDT output is chosen according to the figure of merit $N_{\rm sig}/\sqrt{N_{\rm sig}+N_{\rm bkg}}$, where $N_{\rm sig}$ ($N_{\rm bkg}$) is the expected number of signal (background) events in the signal region. With respect to the previously described selection criteria, this requirement results in a signal efficiency of 96% and a background rejection of 96%, where the latter considers only contributions from combinatorial background.

Decays of b hadrons where one or more of the final-state particles have been misidentified constitute another important background source, referred to as peaking backgrounds. Contributions include decays of the form $B_s^0 \to J/\psi\phi$, $B_s^0 \to \psi(2S)\phi$, $B^0 \to J/\psi K^{*0}$ and $B^0 \to \psi(2S)K^{*0}$, where a hadron is misidentified as a muon and vice versa. Once misidentified, these decays can contaminate the signal q^2 regions. To further suppress these contributions, more stringent particle identification requirements are placed on candidates where the invariant mass of the $\mu^\pm K^\mp$ system under the dimuon mass hypothesis is close to the known J/ψ or $\psi(2S)$ mass [46].

Other sources of peaking background include $\Lambda_b^0 \to pK^-\mu^+\mu^-$ decays, where the proton is misidentified as a kaon, and $B^0 \to K^{*0}(\to K^+\pi^-)\mu^+\mu^-$ decays, where the pion is misidentified as a kaon. The $\Lambda_b^0 \to pK^-\mu^+\mu^-$ decay is additionally suppressed by applying more stringent particle identification criteria if the invariant mass of a candidate under the

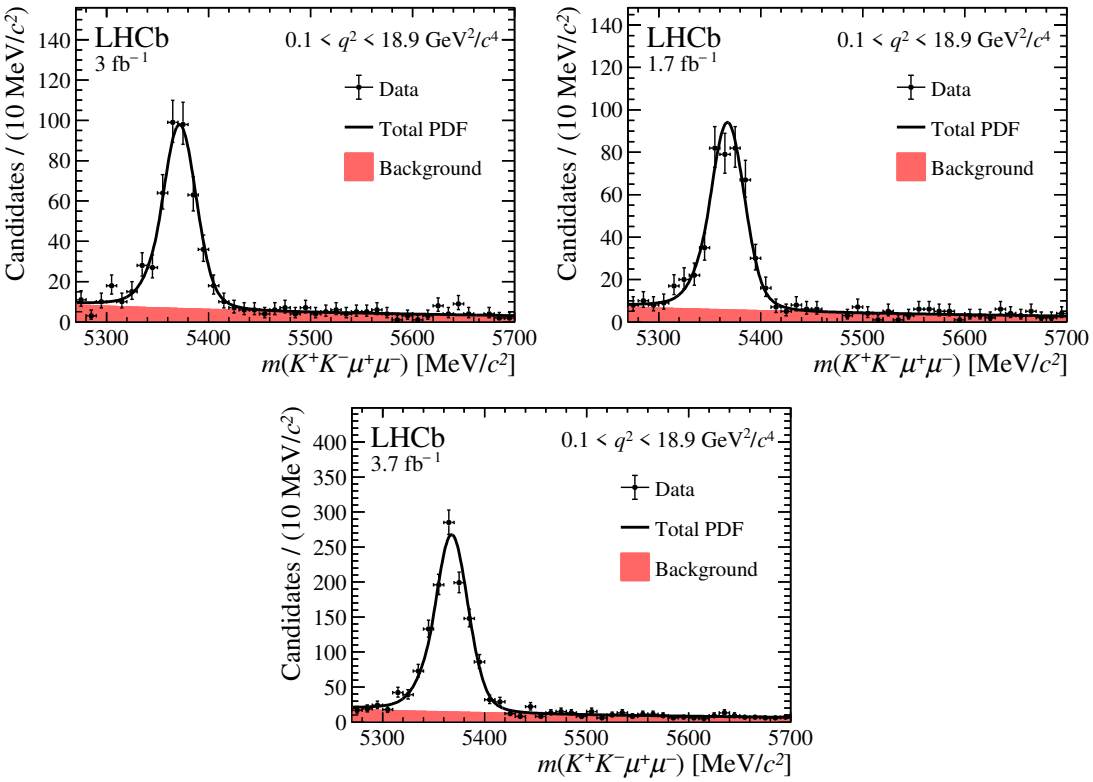

Figure 1: The $m(K^+K^-\mu^+\mu^-)$ distribution for $B_s^0 \to \phi\mu^+\mu^-$ candidates integrated over the $0.1 < q^2 < 0.98\,\text{GeV}^2/c^4$, $1.1 < q^2 < 8\,\text{GeV}^2/c^4$, $11.0 < q^2 < 12.5\,\text{GeV}^2/c^4$ and $15.0 < q^2 < 18.9\,\text{GeV}^2/c^4$ regions for the data-taking periods 2011-2012 (top left), 2016 (top right), and 2017–2018 (bottom). The data are overlaid with the PDF used to describe the $m(K^+K^-\mu^+\mu^-)$ spectrum, fitted separately for each data set.

relevant misidentification hypothesis is close to the known Λ_b^0 mass [46]. No single source of peaking background is found to contribute more than 0.5% of the total signal yield after all selection criteria are applied. Peaking background contributions are therefore neglected in the fit model and a systematic uncertainty is assigned to account for potential residual background pollution.

Figure 1 shows the $m(K^+K^-\mu^+\mu^-)$ distribution for all candidates passing the selection, integrated over the $0.1 < q^2 < 18.9\,\text{GeV}^2/c^4$ region for the separate data sets, excluding the q^2 regions contaminated by the resonant $B_s^0 \to \phi(\to \mu^+\mu^-)\phi$, $B_s^0 \to J/\psi(\to \mu^+\mu^-)\phi$ and $B_s^0 \to \psi(2S)(\to \mu^+\mu^-)\phi$ decays. The data are overlaid with the fitted probability density function (PDF) described in Sec. 4. Signal yields of 408 ± 23, 402 ± 23 and 1120 ± 40 are found for the 2011–2012, 2016 and 2017–2018 data sets, where the uncertainties are statistical only.

4 Angular analysis

The angular observables are determined using an unbinned maximum likelihood fit to the invariant $K^+K^-\mu^+\mu^-$ mass distribution and the three decay angles, θ_l, θ_K, and ϕ. In the q^2 region below $12.5\,\text{GeV}^2/c^4$, the fit is performed separately in narrow q^2 regions of around

$2\,\text{GeV}^2/c^4$ width and in an additional wide q^2 region defined as $[1.1, 6.0]\,\text{GeV}^2/c^4$. Above $15\,\text{GeV}^2/c^4$, a single wide region is used, defined as $[15.0, 18.9]\,\text{GeV}^2/c^4$. A finer binning scheme compared to Ref. [4] is chosen to maximise sensitivity to potential short-distance NP contributions whilst ensuring stable fit behaviour.

The $m(K^+K^-\mu^+\mu^-)$ distribution is included in the fit to improve the separation power between signal and background. The signal component is modelled in $m(K^+K^-\mu^+\mu^-)$ by a sum of two Gaussian functions with a common mean and power-law tails towards the upper or lower mass side [52]. The parameters describing the power-law tails are determined using simulated $B_s^0 \to J/\psi\phi$ events. The parameters describing the widths and the mean of the Gaussian functions are fixed in the signal mode to the values from a fit to $B_s^0 \to J/\psi\phi$ candidates in data. An additional q^2-dependent scaling factor is determined from simulation and applied to the widths of the Gaussian distributions to account for the q^2 dependence of the $m(K^+K^-\mu^+\mu^-)$ invariant-mass resolution. The angular distribution for the signal candidates is parameterised using Eq. 1. The combinatorial background in the $m(K^+K^-\mu^+\mu^-)$ distribution is described using an exponential function and in the angular distributions using a product of first-order Chebyshev polynomials. The factorisation of the background angular distributions is validated using data candidates selected in the upper mass sideband. The fraction of $B_s^0 \to K^+K^-\mu^+\mu^-$ decays with the K^+K^- system in an S-wave configuration, $F_{\rm S}$, is expected to be at the level of 1–2% [53–55]. These contributions are therefore not modelled in the fit and a systematic uncertainty is assigned to account for this choice.

The selection and reconstruction can distort the angular and q^2 distributions observed in data. These effects are described by an angular acceptance, $\epsilon(\cos\theta_\ell, \cos\theta_K, \phi, q^2)$. The acceptance is parameterised using a product of Legendre polynomials P_i of order i according to

$$\epsilon(\cos\theta_\ell, \cos\theta_K, \phi, q^2) = \sum_{k,l,m,n} c_{klmn} P_k(\cos\theta_\ell) P_l(\cos\theta_K) P_m(\phi) P_n(q^2)\,, \tag{2}$$

where the coefficients c_{klmn} are determined on a large sample of simulated $B_s^0 \to \phi\mu^+\mu^-$ events by exploiting the orthogonality of the Legendre polynomials. Given that the acceptance is parameterised in terms of the key degrees of freedom used in the decay description (*i.e.* the three angles and q^2) there is minimal dependency on the model used to simulate the events. The orders used to model the efficiency are $k \leq 4$, $l \leq 2$ ($l \leq 4$ in Run 2), $m \leq 6$ and $n \leq 7$ in $\cos\theta_\ell$, $\cos\theta_K$, ϕ and q^2, respectively. Where different sets of acceptance orders give a similar description of the acceptance function, the set of lowest orders is chosen. Given the flavour-symmetric final state, only even orders are considered in the description of the three decay angles. The choice of orders used to describe the angular acceptance is assessed as a source of systematic uncertainty.

In the narrow q^2 regions, the PDF describing the signal candidates is constructed from the product of the acceptance function evaluated at the median of the q^2 region and the signal fit model. For the wide q^2 regions, the acceptance is taken into account by weighting each event by the inverse efficiency. The shape of the angular acceptance is found to vary according to the data-taking conditions. The different trigger thresholds during the 2016 and 2017–2018 data-taking periods require the Run 2 data to be further separated. The angular acceptance is therefore derived separately for the 2011–2012, 2016 and 2017–2018 data sets. The data are split according to these periods and a simultaneous fit is performed. In the fit, the angular observables and angular background parameters

are shared across the three data sets. The sharing of the angular background parameters improves the fit behaviour and the resulting small bias due to this choice is added as a systematic uncertainty. All other nuisance parameters are determined independently for each data set. In order to avoid experimenter's bias, all decisions regarding the fit strategy and candidate selection were made before the results were examined.

Pseudoexperiments, generated using the results of the best fit to data, are used to assess the bias and coverage of the simultaneous fit. The majority of observables have a bias of less than 10% of the statistical uncertainty. The observables S_3 and S_4 in the q^2 region $[4.0, 6.0]\,\mathrm{GeV}^2/c^4$ and A_{FB}^{CP} in the q^2 region $[0.1, 0.98]\,\mathrm{GeV}^2/c^4$ exhibit a fit bias at the level of 15% of the statistical uncertainty. An additional systematic uncertainty equal to the size of the fit bias is assigned for all observables and the statistical uncertainty is corrected to account for any under- or over-coverage, which is at the level of 14% or less.

The angular acceptance corrections for each data set are validated using both fits to $B_s^0 \to J/\psi\phi$ candidates and fits to simulated $B_s^0 \to \phi\mu^+\mu^-$ candidates, where the latter are generated according to a physics model using inputs from Ref. [56]. The angular observables extracted from fits to $B_s^0 \to J/\psi\phi$ candidates are in good agreement with previous measurements [54, 55]. In addition, the angular observables extracted from fits to simulated events are in good agreement with the values used in their generation.

5 Results

The angular distributions for the combined 2011–2012, 2016 and 2017–2018 data set are shown in Fig. 2 for all candidates in the $[1.1, 6]\,\mathrm{GeV}^2/c^4$ q^2 region and for candidates within $\pm 50\,\mathrm{MeV}/c^2$ of the known B_s^0 mass. The data are overlaid with the projection of the fitted PDF, combined across the data sets. The fit projections for all q^2 regions and individual data sets are provided in Appendix A.

The numerical results for the angular observables are given in Table 1, including systematic uncertainties as discussed in Sec. 6. The linear-correlation matrices for the angular observables are provided in Tables 3, 4 and 5 in Appendix B. A graphical comparison of the results with the SM predictions [23–26] is shown in Fig. 3. Overall, the results are in good agreement with the SM predictions, with the *CP* asymmetries compatible with zero as expected in the SM. For the *CP* averages, a mild tension in F_{L} is observed at low q^2, where the data are found to lie below the SM prediction.

To determine the compatibility of the angular observables with the SM, the `flavio` software package [24] is used. The Wilson coefficient representing the real part of the $bs\mu\mu$ vector coupling, $\mathcal{R}e(\mathcal{C}_9)$, is varied in a fit of the *CP*-averaged angular observables F_{L}, S_3, S_4 and S_7 in the q^2 regions $[0.1, 0.98]$, $[1.1, 4.0]$, $[4.0, 6.0]$ and $[15, 18.9]\,\mathrm{GeV}^2/c^4$. The $[6.0, 8.0]$ and $[11.0, 12.5]\,\mathrm{GeV}^2/c^4$ regions are excluded from the fit as they are particularly sensitive to long-distance effects from charmonium resonances, which cannot currently be calculated from first principles in the SM [30]. The asymmetries are excluded as they offer little sensitivity to $\mathcal{R}e(\mathcal{C}_9)$. The best fit value is given by $\Delta\mathcal{R}e(\mathcal{C}_9) = -1.3\,^{+0.7}_{-0.6}$ and is preferred over the SM hypothesis ($\Delta\mathcal{R}e(\mathcal{C}_9) = 0$) at the level of $1.9\,\sigma$.

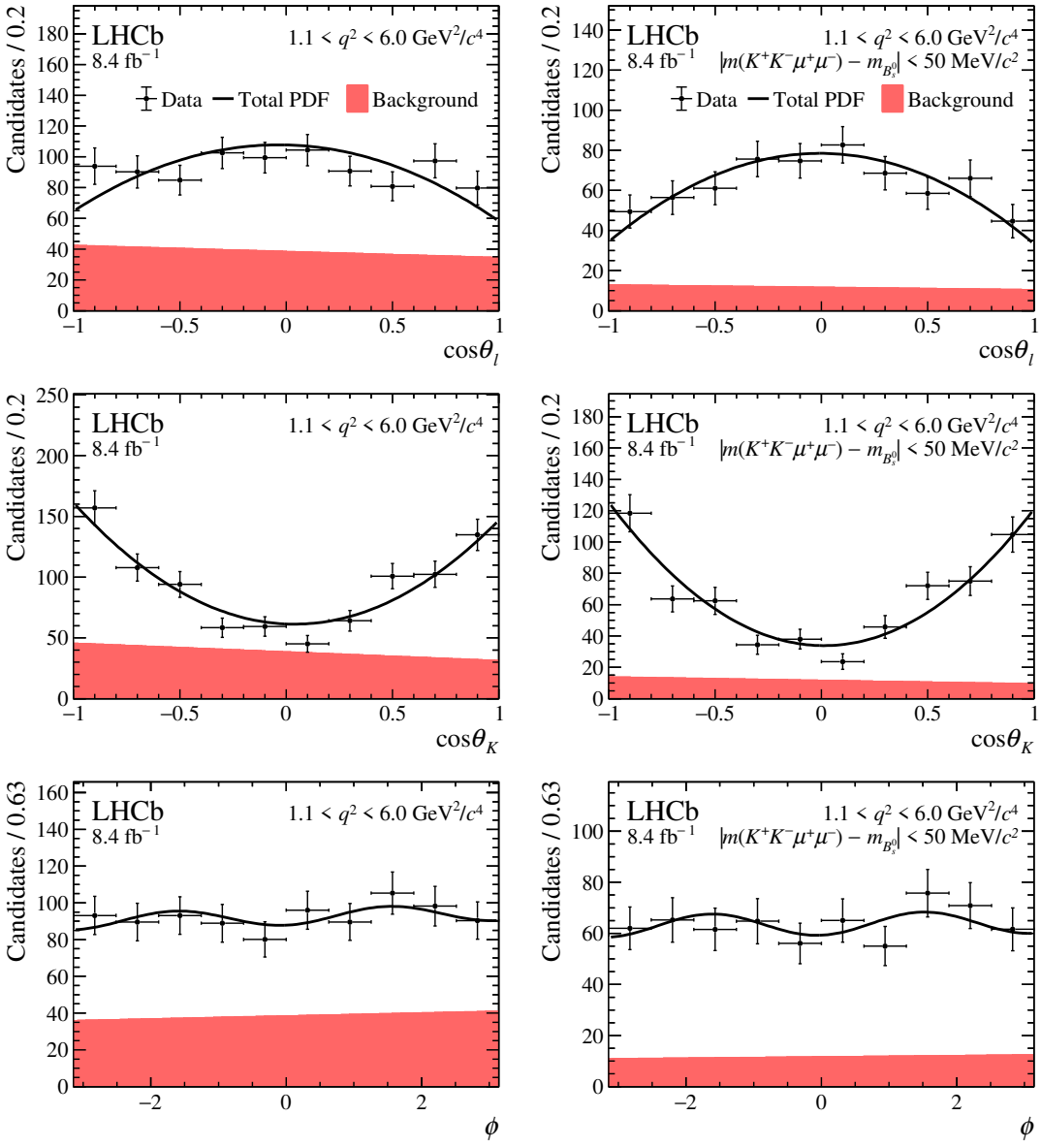

Figure 2: Angular projections in the region $1.1 < q^2 < 6.0\,\text{GeV}^2/c^4$ for the combined 2011–2012, 2016 and 2017–2018 data sets. The data are overlaid with the projection of the combined PDF. The red shaded area indicates the background component and the solid black line the total PDF. The angular projections are given for candidates in (left) the entire mass region used to determine the observables in this paper and (right) the signal mass window $\pm 50\,\text{MeV}/c^2$ around the known B_s^0 mass.

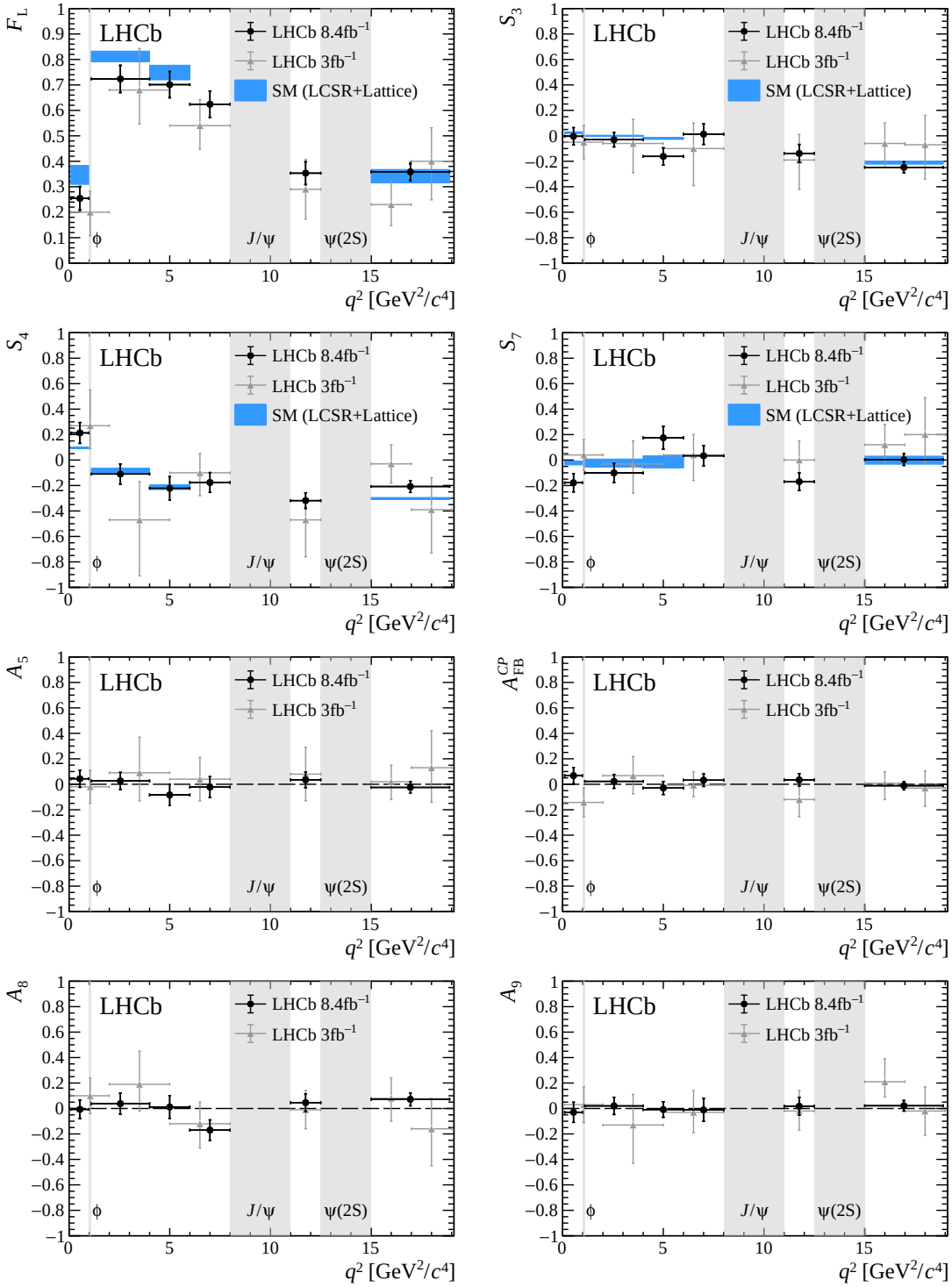

Figure 3: *CP*-averaged angular observables $F_{\rm L}$ and $S_{3,4,7}$ and *CP*-asymmetries $A_{\rm FB}^{CP}$ and $A_{5,8,9}$ shown by black crosses, overlaid with the SM prediction [23–26] as blue boxes, where available. The grey crosses indicate the results from Ref. [4]. The grey bands indicate the regions of the charmonium resonances and the $B_s^0 \to \phi\phi$ region.

Table 1: *CP* averages $F_{\rm L}$ and $S_{3,4,7}$ and *CP* asymmetries $A_{\rm FB}^{CP}$ and $A_{5,8,9}$ obtained from the maximum likelihood fit. The first uncertainty is statistical and the second is the total systematic uncertainty, as described in Sec. 6.

q^2 [GeV$^2/c^4$]	$F_{\rm L}$	S_3	S_4	S_7
$[0.1, 0.98]$	$0.254 \pm 0.045 \pm 0.017$	$-0.004 \pm 0.068 \pm 0.014$	$0.213 \pm 0.082 \pm 0.005$	$-0.178 \pm 0.072 \pm 0.001$
$[1.1, 4.0]$	$0.723 \pm 0.053 \pm 0.015$	$-0.030 \pm 0.057 \pm 0.004$	$-0.110 \pm 0.079 \pm 0.002$	$-0.101 \pm 0.075 \pm 0.001$
$[4.0, 6.0]$	$0.701 \pm 0.050 \pm 0.016$	$-0.162 \pm 0.067 \pm 0.012$	$-0.222 \pm 0.092 \pm 0.010$	$0.175 \pm 0.089 \pm 0.003$
$[6.0, 8.0]$	$0.624 \pm 0.051 \pm 0.012$	$0.013 \pm 0.080 \pm 0.009$	$-0.176 \pm 0.078 \pm 0.006$	$0.033 \pm 0.081 \pm 0.002$
$[11.0, 12.5]$	$0.353 \pm 0.044 \pm 0.012$	$-0.138 \pm 0.071 \pm 0.013$	$-0.319 \pm 0.061 \pm 0.008$	$-0.170 \pm 0.069 \pm 0.000$
$[1.1, 6.0]$	$0.715 \pm 0.036 \pm 0.013$	$-0.083 \pm 0.047 \pm 0.006$	$-0.155 \pm 0.058 \pm 0.004$	$0.020 \pm 0.059 \pm 0.001$
$[15.0, 18.9]$	$0.359 \pm 0.031 \pm 0.019$	$-0.247 \pm 0.042 \pm 0.014$	$-0.208 \pm 0.047 \pm 0.006$	$0.003 \pm 0.046 \pm 0.002$

q^2 [GeV$^2/c^4$]	A_5	$A_{\rm FB}^{CP}$	A_8	A_9
$[0.1, 0.98]$	$0.043 \pm 0.067 \pm 0.001$	$0.068 \pm 0.064 \pm 0.009$	$-0.007 \pm 0.073 \pm 0.004$	$-0.030 \pm 0.079 \pm 0.001$
$[1.1, 4.0]$	$0.026 \pm 0.067 \pm 0.002$	$0.023 \pm 0.054 \pm 0.001$	$0.038 \pm 0.082 \pm 0.001$	$0.020 \pm 0.068 \pm 0.001$
$[4.0, 6.0]$	$-0.084 \pm 0.084 \pm 0.003$	$-0.030 \pm 0.051 \pm 0.002$	$0.012 \pm 0.090 \pm 0.002$	$-0.008 \pm 0.061 \pm 0.001$
$[6.0, 8.0]$	$-0.022 \pm 0.082 \pm 0.001$	$0.032 \pm 0.049 \pm 0.001$	$-0.170 \pm 0.080 \pm 0.002$	$-0.012 \pm 0.090 \pm 0.001$
$[11.0, 12.5]$	$0.035 \pm 0.063 \pm 0.001$	$0.034 \pm 0.048 \pm 0.001$	$0.046 \pm 0.070 \pm 0.002$	$0.017 \pm 0.071 \pm 0.001$
$[1.1, 6.0]$	$-0.007 \pm 0.051 \pm 0.001$	$0.006 \pm 0.036 \pm 0.001$	$0.016 \pm 0.062 \pm 0.001$	$0.009 \pm 0.046 \pm 0.001$
$[15.0, 18.9]$	$-0.025 \pm 0.043 \pm 0.001$	$-0.011 \pm 0.033 \pm 0.001$	$0.072 \pm 0.051 \pm 0.002$	$0.021 \pm 0.042 \pm 0.001$

6 Systematic uncertainties

Systematic effects may change the measured angular observables. The size of these effects is determined using high-yield pseudoexperiments, generated using an alternative PDF which encodes the systematic effect under study. The pseudoexperiments are fitted with both the default and alternative PDFs, and the resulting difference in angular observables is assigned as a systematic uncertainty. Each systematic effect is studied using approximately one hundred million generated events.

The simulated samples used to derive the default acceptance are produced according to the phase space of the three-body $B_s^0 \to \phi\mu^+\mu^-$ decay with the lifetime difference between the B_s^0 and $\overline{B}_s^0$ system, $\Delta\Gamma_s$, set to zero. A systematic uncertainty is determined by weighting the angular, q^2 and B_s^0 lifetime distributions of simulated events to an alternative model description, in which the value for $\Delta\Gamma_s/\Gamma_s$ is taken as 0.17 [57] and the $B_s^0 \to \phi\mu^+\mu^-$ decay is described using a more realistic physics model with form factor calculations taken from Refs. [23–26].

As the angular observables are measured integrated over the B_s^0 decay time, neglecting the B_s^0 decay time dependence of the acceptance induces an additional source of bias. The size of this effect remains small compared to the statistical uncertainty and is accounted for with a systematic uncertainty.

To assess the systematic uncertainty associated with the description of the angular background distribution, pseudoexperiments are generated using second-order Chebyshev polynomials, the coefficients for which are obtained from a fit to candidates in the upper mass sideband. Similarly, the impact of sharing the angular background parameters across data sets is determined by generating pseudoexperiments using first order Chebyshev polynomials with coefficients derived separately for each data set.

Table 2: Sources of the systematic uncertainties associated with the angular observables. As the size of a systematic effect can vary strongly depending on the observable and q^2 region in question, only the magnitude of the largest systematic uncertainty across all regions, rounded up to the next multiple of 0.005, is indicated.

Systematic source	$F_{\rm L}$	$S_{3,4,7}$	$A_{5,8,9}, A_{\rm FB}^{CP}$
Physics model	< 0.015	< 0.015	< 0.005
Time integration	< 0.010	< 0.010	< 0.005
Fit bias	< 0.005	< 0.015	< 0.010
Angular background model	< 0.015	< 0.005	< 0.005
Simulation corrections	< 0.015	< 0.005	< 0.005
S-wave and peaking bkg.	< 0.010	< 0.010	< 0.005
Acceptance order	< 0.010	< 0.005	< 0.005
Simulation statistics	< 0.010	< 0.005	< 0.005
Signal mass model	< 0.005	< 0.005	< 0.005
q^2 evaluation point	< 0.005	< 0.005	< 0.005

To evaluate the impact of the corrections to the track multiplicity, B_s^0 $p_{\rm T}$ spectrum and hardware trigger response in simulated events on the angular observables, the angular acceptance is rederived, each time removing a correction. The largest resulting deviation in a given angular observable is assigned as a systematic uncertainty. For the particle identification response, the corrections are determined using an alternative model and a new angular acceptance is rederived.

To account for neglected $B_s^0 \to K^+K^-\mu^+\mu^-$ decays, where the K^+K^- system is in an S-wave configuration, pseudoexperiments are generated according to the combined P- and S-wave decay rate, where $F_{\rm S}$ is conservatively taken to be 2%. The pseudoexperiments are fitted with the default model and the resulting shift in the angular observables is assigned as a systematic uncertainty. The impact of peaking background contributions is assessed in a similar fashion by injecting additional events drawn from the reconstructed B_s^0 mass and angular distributions of the background in question.

The influence of the choice for the maximum order of the Legendre polynomials used in the acceptance parameterisation is evaluated by rederiving the acceptance using a higher order. Further sources of systematic uncertainty include the size of the simulated samples used to derive the acceptance, the evaluation of the acceptance at a single point in q^2 for the narrow q^2 regions and the signal mass model, all of which yield negligible contributions to the overall systematic uncertainty.

The systematic uncertainties are summarised in Table 2. As the size of a systematic effect can vary strongly depending on the observable and q^2 region in question, only the magnitude of the largest systematic uncertainty across all regions, rounded up to the next multiple of 0.005, is indicated.

7 Conclusions

This paper presents an angular analysis of the $B_s^0 \to \phi\mu^+\mu^-$ decay using pp collisions corresponding to 8.4 fb^{-1} of data recorded by the LHCb experiment during the Run 1 and Run 2 data-taking periods. The angular observables are extracted using an unbinned maximum likelihood fit to the angular distributions of untagged $B_s^0 \to \phi\mu^+\mu^-$ decays in regions of the square of the dimuon mass, q^2. The results in this paper constitute the most precise measurement of the $B_s^0 \to \phi\mu^+\mu^-$ angular observables to date, with an approximate two-fold increase in sensitivity compared to the results of Ref. [4], which are superseded by this paper. The results are found to be compatible with SM predictions.

Acknowledgements

We express our gratitude to our colleagues in the CERN accelerator departments for the excellent performance of the LHC. We thank the technical and administrative staff at the LHCb institutes. We acknowledge support from CERN and from the national agencies: CAPES, CNPq, FAPERJ and FINEP (Brazil); MOST and NSFC (China); CNRS/IN2P3 (France); BMBF, DFG and MPG (Germany); INFN (Italy); NWO (Netherlands); MNiSW and NCN (Poland); MEN/IFA (Romania); MSHE (Russia); MICINN (Spain); SNSF and SER (Switzerland); NASU (Ukraine); STFC (United Kingdom); DOE NP and NSF (USA). We acknowledge the computing resources that are provided by CERN, IN2P3 (France), KIT and DESY (Germany), INFN (Italy), SURF (Netherlands), PIC (Spain), GridPP (United Kingdom), RRCKI and Yandex LLC (Russia), CSCS (Switzerland), IFIN-HH (Romania), CBPF (Brazil), PL-GRID (Poland) and NERSC (USA). We are indebted to the communities behind the multiple open-source software packages on which we depend. Individual groups or members have received support from ARC and ARDC (Australia); AvH Foundation (Germany); EPLANET, Marie Skłodowska-Curie Actions and ERC (European Union); A*MIDEX, ANR, IPhU and Labex P2IO, and Région Auvergne-Rhône-Alpes (France); Key Research Program of Frontier Sciences of CAS, CAS PIFI, CAS CCEPP, Fundamental Research Funds for the Central Universities, and Sci. & Tech. Program of Guangzhou (China); RFBR, RSF and Yandex LLC (Russia); GVA, XuntaGal and GENCAT (Spain); the Leverhulme Trust, the Royal Society and UKRI (United Kingdom).

References

[1] LHCb collaboration, R. Aaij *et al.*, *Differential branching fraction and angular analysis of the decay* $B_s^0 \to \phi\mu^+\mu^-$, JHEP **07** (2013) 084, arXiv:1305.2168.

[2] LHCb collaboration, R. Aaij *et al.*, *Differential branching fractions and isospin asymmetries of* $B \to K^{(*)}\mu^+\mu^-$ *decays*, JHEP **06** (2014) 133, arXiv:1403.8044.

[3] LHCb collaboration, R. Aaij *et al.*, *Differential branching fraction and angular analysis of* $\Lambda_b^0 \to \Lambda\mu^+\mu^-$ *decays*, JHEP **06** (2015) 115, Erratum ibid. **09** (2018) 145, arXiv:1503.07138.

[4] LHCb collaboration, R. Aaij *et al.*, *Angular analysis and differential branching fraction of the decay* $B_s^0 \to \phi\mu^+\mu^-$, JHEP **09** (2015) 179, arXiv:1506.08777.

[5] LHCb collaboration, R. Aaij *et al.*, *Measurements of the S-wave fraction in* $B^0 \to K^+\pi^-\mu^+\mu^-$ *decays and the* $B^0 \to K^*(892)^0\mu^+\mu^-$ *differential branching fraction*, JHEP **11** (2016) 047, Erratum ibid. **04** (2017) 142, arXiv:1606.04731.

[6] LHCb collaboration, R. Aaij *et al.*, *Branching fraction measurements of the rare* $B_s^0 \to \phi\mu^+\mu^-$ *and* $B_s^0 \to f_2'(1525)\mu^+\mu^-$ *decays*, arXiv:2105.14007, submitted to PRL.

[7] LHCb collaboration, R. Aaij *et al.*, *Angular analysis of the* $B^0 \to K^{*0}\mu^+\mu^-$ *decay using* $3\,fb^{-1}$ *of integrated luminosity*, JHEP **02** (2016) 104, arXiv:1512.04442.

[8] LHCb collaboration, R. Aaij *et al.*, *Measurement of CP-averaged observables in the* $B^0 \to K^{*0}\mu^+\mu^-$ *decay*, Phys. Rev. Lett. **125** (2020) 011802, arXiv:2003.04831.

[9] LHCb collaboration, R. Aaij *et al.*, *Angular analysis of the* $B^+ \to K^{*+}\mu^+\mu^-$ *decay*, Phys. Rev. Lett. **126** (2021) 161802, arXiv:2012.13241.

[10] ATLAS collaboration, M. Aaboud *et al.*, *Angular analysis of* $B_d^0 \to K^*\mu^+\mu^-$ *decays in pp collisions at* $\sqrt{s} = 8$ *TeV with the ATLAS detector*, JHEP **10** (2018) 047, arXiv:1805.04000.

[11] CMS collaboration, V. Khachatryan *et al.*, *Angular analysis of the decay* $B^0 \to K^{*0}\mu^+\mu^-$ *from pp collisions at* $\sqrt{s} = 8$ *TeV*, Phys. Lett. **B753** (2016) 424, arXiv:1507.08126.

[12] CMS collaboration, A. M. Sirunyan *et al.*, *Measurement of angular parameters from the decay* $B^0 \to K^{*0}\mu^+\mu^-$ *in proton-proton collisions at* $\sqrt{s} = 8$ *TeV*, Phys. Lett. **B781** (2018) 517, arXiv:1710.02846.

[13] Belle collaboration, S. Wehle *et al.*, *Lepton-Flavor-Dependent Angular Analysis of* $B \to K^*\ell^+\ell^-$, Phys. Rev. Lett. **118** (2017) 111801, arXiv:1612.05014.

[14] LHCb collaboration, R. Aaij *et al.*, *Test of lepton universality using* $B^+ \to K^+\ell^+\ell^-$ *decays*, Phys. Rev. Lett. **113** (2014) 151601, arXiv:1406.6482.

[15] LHCb collaboration, R. Aaij *et al.*, *Test of lepton universality with* $B^0 \to K^{*0}\ell^+\ell^-$ *decays*, JHEP **08** (2017) 055, arXiv:1705.05802.

[16] LHCb collaboration, R. Aaij *et al.*, *Search for lepton-universality violation in* $B^+ \to K^+\ell^+\ell^-$ *decays*, Phys. Rev. Lett. **122** (2019) 191801, arXiv:1903.09252.

[17] LHCb collaboration, R. Aaij *et al.*, *Test of lepton universality using* $\Lambda_b^0 \to pK^-\ell^+\ell^-$ *decays*, JHEP **05** (2020) 040, arXiv:1912.08139.

[18] LHCb collaboration, R. Aaij *et al.*, *Test of lepton universality in beauty-quark decays*, arXiv:2103.11769, submitted to Nature Physics.

[19] BaBar collaboration, J. P. Lees *et al.*, *Measurement of Branching Fractions and Rate Asymmetries in the Rare Decays* $B \to K^{(*)}l^+l^-$, Phys. Rev. **D86** (2012) 032012, arXiv:1204.3933.

[20] Belle collaboration, S. Choudhury *et al.*, *Test of lepton flavor universality and search for lepton flavor violation in $B \to K\ell\ell$ decays*, JHEP **03** (2021) 105, arXiv:1908.01848.

[21] Belle collaboration, A. Abdesselam *et al.*, *Test of Lepton-Flavor Universality in $B \to K^*\ell^+\ell^-$ Decays at Belle*, Phys. Rev. Lett. **126** (2021) 161801, arXiv:1904.02440.

[22] W. Altmannshofer and D. M. Straub, *New physics in $b \to s$ transitions after LHC run 1*, Eur. Phys. J. **C75** (2015) 382, arXiv:1411.3161.

[23] A. Bharucha, D. M. Straub, and R. Zwicky, *$B \to V\ell^+\ell^-$ in the Standard Model from light-cone sum rules*, JHEP **08** (2016) 098, arXiv:1503.05534.

[24] D. M. Straub, *flavio: a Python package for flavour and precision phenomenology in the Standard Model and beyond*, arXiv:1810.08132.

[25] R. R. Horgan, Z. Liu, S. Meinel, and M. Wingate, *Calculation of $B^0 \to K^{*0}\mu^+\mu^-$ and $B_s^0 \to \phi\mu^+\mu^-$ observables using form factors from lattice QCD*, Phys. Rev. Lett. **112** (2014) 212003, arXiv:1310.3887.

[26] R. R. Horgan, Z. Liu, S. Meinel, and M. Wingate, *Rare B decays using lattice QCD form factors*, PoS **LATTICE2014** (2015) 372, arXiv:1501.00367.

[27] LHCb collaboration, R. Aaij *et al.*, *Measurement of the b-quark production cross-section in 7 and 13 TeV pp collisions*, Phys. Rev. Lett. **118** (2017) 052002, Erratum ibid. **119** (2017) 169901, arXiv:1612.05140.

[28] LHCb collaboration, R. Aaij *et al.*, *Measurement of the $B^\pm$ production cross-section in pp collisions at $\sqrt{s}$ =7 and 13 TeV*, JHEP **12** (2017) 026, arXiv:1710.04921.

[29] S. Descotes-Genon and J. Virto, *Time dependence in $B \to V\ell\ell$ decays*, JHEP **04** (2015) 045, Erratum ibid. **07** (2015) 049, arXiv:1502.05509.

[30] W. Altmannshofer *et al.*, *Symmetries and Asymmetries of $B \to K^*\mu^+\mu^-$ Decays in the Standard Model and Beyond*, JHEP **01** (2009) 019, arXiv:0811.1214.

[31] C. Bobeth, G. Hiller, and G. Piranishvili, *CP Asymmetries in $\bar{B} \to \bar{K}^*(\to \bar{K}\pi)\bar{\ell}\ell$ and Untagged $\bar{B}_s$, $B_s \to \phi(\to K^+K^-)\bar{\ell}\ell$ Decays at NLO*, JHEP **07** (2008) 106, arXiv:0805.2525.

[32] LHCb collaboration, A. A. Alves Jr. *et al.*, *The LHCb detector at the LHC*, JINST **3** (2008) S08005.

[33] LHCb collaboration, R. Aaij *et al.*, *LHCb detector performance*, Int. J. Mod. Phys. **A30** (2015) 1530022, arXiv:1412.6352.

[34] R. Aaij *et al.*, *Performance of the LHCb Vertex Locator*, JINST **9** (2014) P09007, arXiv:1405.7808.

[35] R. Arink *et al.*, *Performance of the LHCb Outer Tracker*, JINST **9** (2014) P01002, arXiv:1311.3893.

[36] P. d'Argent *et al.*, *Improved performance of the LHCb Outer Tracker in LHC Run 2*, JINST **12** (2017) P11016, arXiv:1708.00819.

[37] M. Adinolfi *et al.*, *Performance of the LHCb RICH detector at the LHC*, Eur. Phys. J. **C73** (2013) 2431, arXiv:1211.6759.

[38] A. A. Alves Jr. *et al.*, *Performance of the LHCb muon system*, JINST **8** (2013) P02022, arXiv:1211.1346.

[39] R. Aaij *et al.*, *The LHCb trigger and its performance in 2011*, JINST **8** (2013) P04022, arXiv:1211.3055.

[40] T. Sjöstrand, S. Mrenna, and P. Skands, *A brief introduction to PYTHIA 8.1*, Comput. Phys. Commun. **178** (2008) 852, arXiv:0710.3820; T. Sjöstrand, S. Mrenna, and P. Skands, *PYTHIA 6.4 physics and manual*, JHEP **05** (2006) 026, arXiv:hep-ph/0603175.

[41] I. Belyaev *et al.*, *Handling of the generation of primary events in Gauss, the LHCb simulation framework*, J. Phys. Conf. Ser. **331** (2011) 032047.

[42] D. J. Lange, *The EvtGen particle decay simulation package*, Nucl. Instrum. Meth. **A462** (2001) 152.

[43] N. Davidson, T. Przedzinski, and Z. Was, *PHOTOS interface in C++: Technical and physics documentation*, Comp. Phys. Comm. **199** (2016) 86, arXiv:1011.0937.

[44] Geant4 collaboration, J. Allison *et al.*, *Geant4 developments and applications*, IEEE Trans. Nucl. Sci. **53** (2006) 270; Geant4 collaboration, S. Agostinelli *et al.*, *Geant4: A simulation toolkit*, Nucl. Instrum. Meth. **A506** (2003) 250.

[45] M. Clemencic *et al.*, *The LHCb simulation application, Gauss: Design, evolution and experience*, J. Phys. Conf. Ser. **331** (2011) 032023.

[46] Particle Data Group, P. A. Zyla *et al.*, *Review of particle physics*, Prog. Theor. Exp. Phys. **2020** (2020) 083C01.

[47] L. Breiman, J. H. Friedman, R. A. Olshen, and C. J. Stone, *Classification and regression trees*, Wadsworth international group, Belmont, California, USA, 1984.

[48] Y. Freund and R. E. Schapire, *A decision-theoretic generalization of on-line learning and an application to boosting*, J. Comput. Syst. Sci. **55** (1997) 119.

[49] H. Voss, A. Hoecker, J. Stelzer, and F. Tegenfeldt, *TMVA - Toolkit for Multivariate Data Analysis with ROOT*, PoS **ACAT** (2007) 040; A. Hoecker *et al.*, *TMVA 4 — Toolkit for Multivariate Data Analysis with ROOT. Users Guide.*, arXiv:physics/0703039.

[50] A. Blum, A. Kalai, and J. Langford, *Beating the hold-out: Bounds for k-fold and progressive cross-validation*, in *Proceedings of the Twelfth Annual Conference on Computational Learning Theory*, COLT '99, (New York, NY, USA), 203–208, ACM, 1999.

[51] M. Pivk and F. R. Le Diberder, *sPlot: A statistical tool to unfold data distributions*, Nucl. Instrum. Meth. **A555** (2005) 356, arXiv:physics/0402083.

[52] T. Skwarnicki, *A study of the radiative cascade transitions between the Upsilon-prime and Upsilon resonances*, PhD thesis, Institute of Nuclear Physics, Krakow, 1986, DESY-F31-86-02.

[53] LHCb collaboration, R. Aaij *et al.*, *Amplitude analysis and branching fraction measurement of* $\overline{B}{}^0_s \to J/\psi K^+K^-$, Phys. Rev. **D87** (2013) 072004, arXiv:1302.1213.

[54] LHCb collaboration, R. Aaij *et al.*, *Precision measurement of CP violation in* $B^0_s \to J/\psi K^+K^-$ *decays*, Phys. Rev. Lett. **114** (2015) 041801, arXiv:1411.3104.

[55] LHCb collaboration, R. Aaij *et al.*, *Updated measurement of time-dependent CP-violating observables in* $B^0_s \to J/\psi K^+K^-$ *decays*, Eur. Phys. J. **C79** (2019) 706, Erratum ibid. **C80** (2020) 601, arXiv:1906.08356.

[56] P. Ball and R. Zwicky, $B_{d,s} \to \rho, \omega, K^*, \phi$ *decay form-factors from light-cone sum rules revisited*, Phys. Rev. **D71** (2005) 014029, arXiv:hep-ph/0412079.

[57] Particle Data Group, K. A. Olive *et al.*, *Review of particle physics*, Chin. Phys. **C38** (2014) 090001.

Appendices

A Fit projections for the rare decay $B_s^0 \to \phi\mu^+\mu^-$

The mass distributions for the combined 2011–2012, 2016 and 2017–2018 data sets for each q^2 region are shown in Fig. 4. The corresponding angular distributions are shown in Figs. 5–11, for all candidates and the candidates within the signal mass region $\pm 50\,\mathrm{MeV}/c^2$ around the known B_s^0 mass. The data are overlaid with the projections of the fitted PDF, combined across the data sets. The projections of the mass and angular distributions, for each data set and q^2 region separately, are shown in Figs. 12–32. All three data sets used in this analysis are fitted simultaneously.

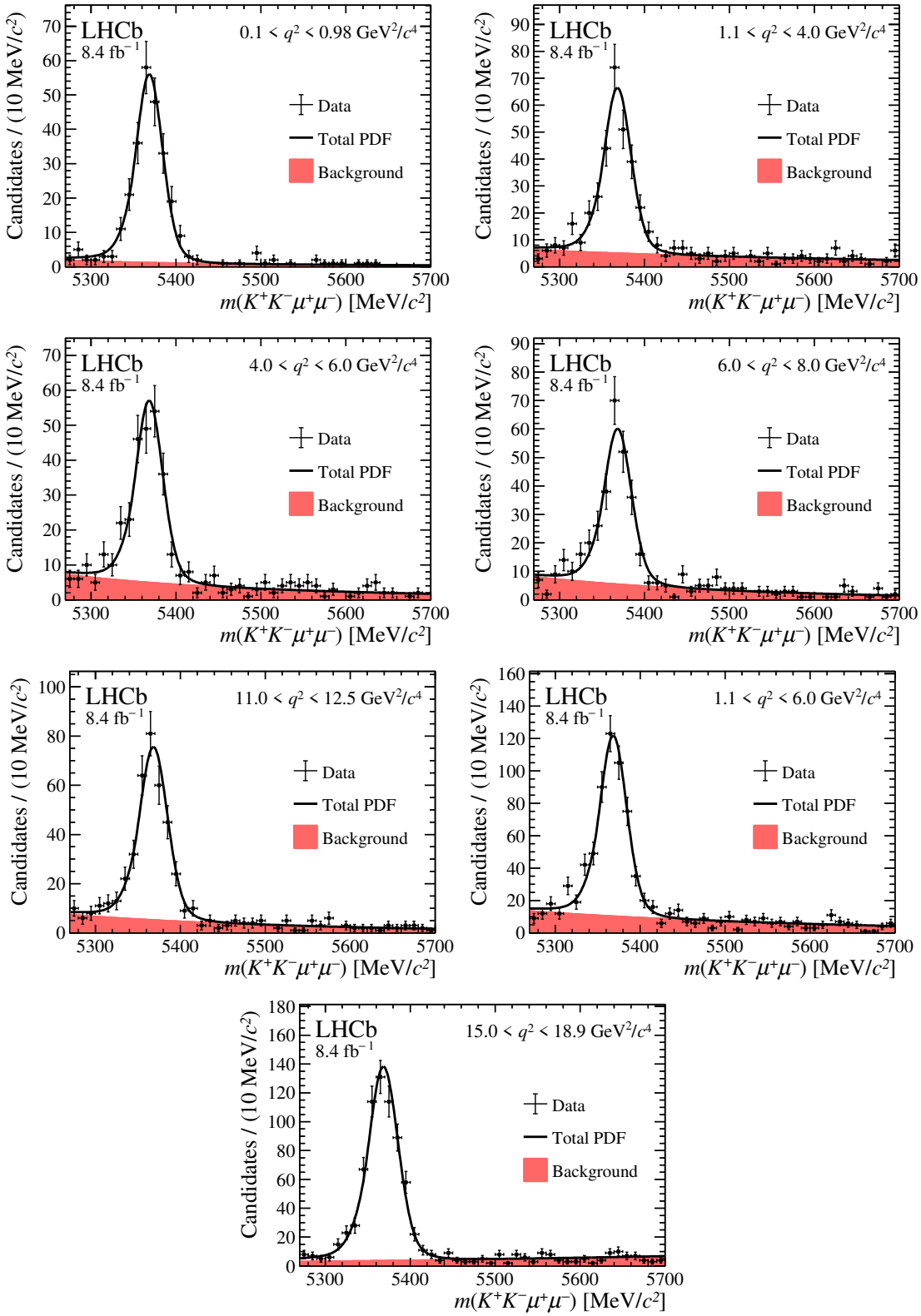

Figure 4: Mass distributions of $B_s^0 \to \phi\mu^+\mu^-$ candidates in the different q^2 regions for the combined 2011–2012, 2016 and 2017–2018 data sets. The data are overlaid with the projection of the combined PDF. The red shaded area indicates the background component and the solid black line the total PDF.

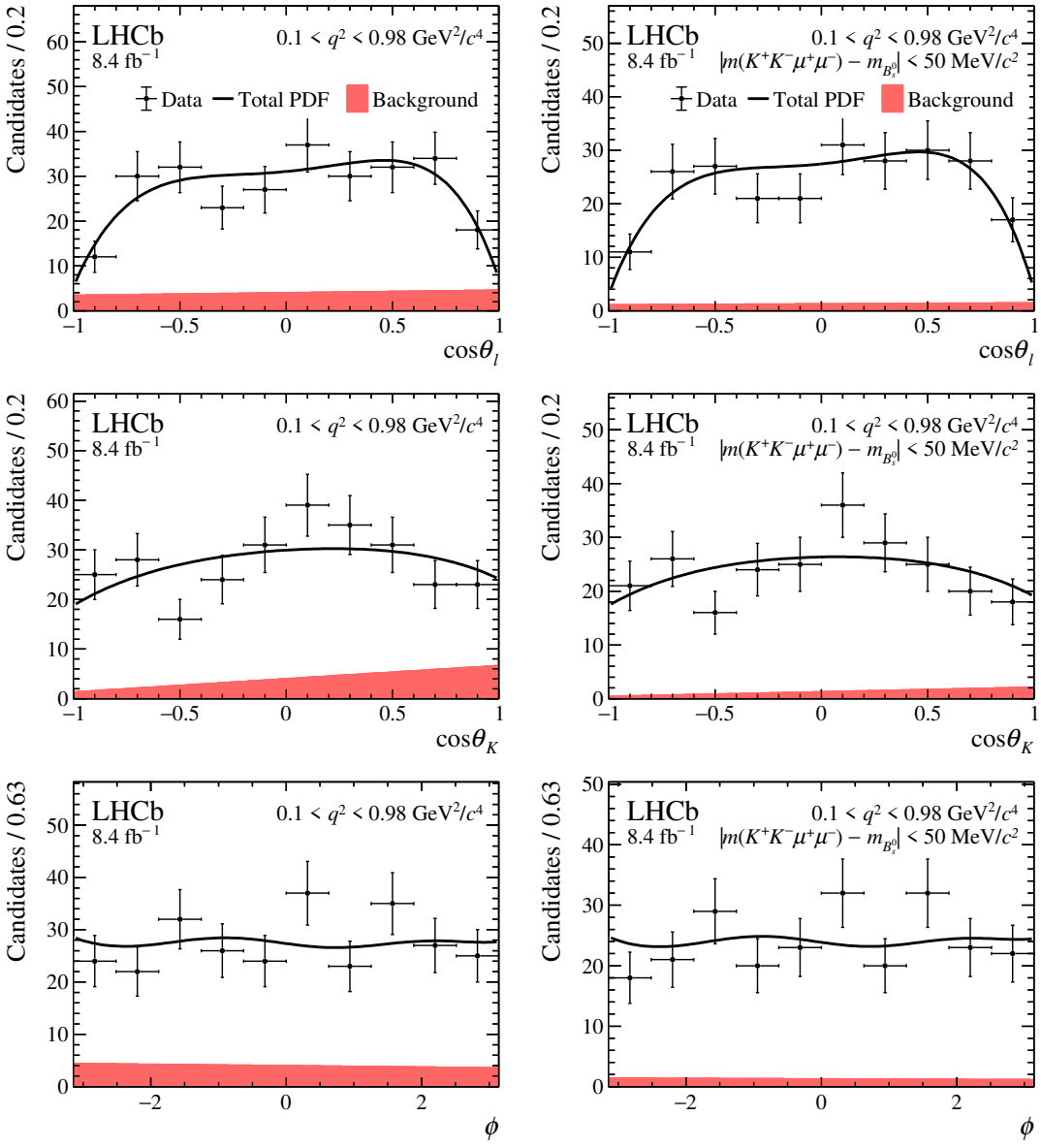

Figure 5: Projections in the region $0.1 < q^2 < 0.98\,\text{GeV}^2/c^4$ for the angular distributions of the combined 2011–2012, 2016 and 2017–2018 data sets. The data are overlaid with the projection of the combined PDF. The red shaded area indicates the background component and the solid black line the total PDF. The angular projections are given for candidates in (left) the entire mass region used to determine the observables in this paper and (right) the signal mass window $\pm 50\,\text{MeV}/c^2$ around the known B_s^0 mass.

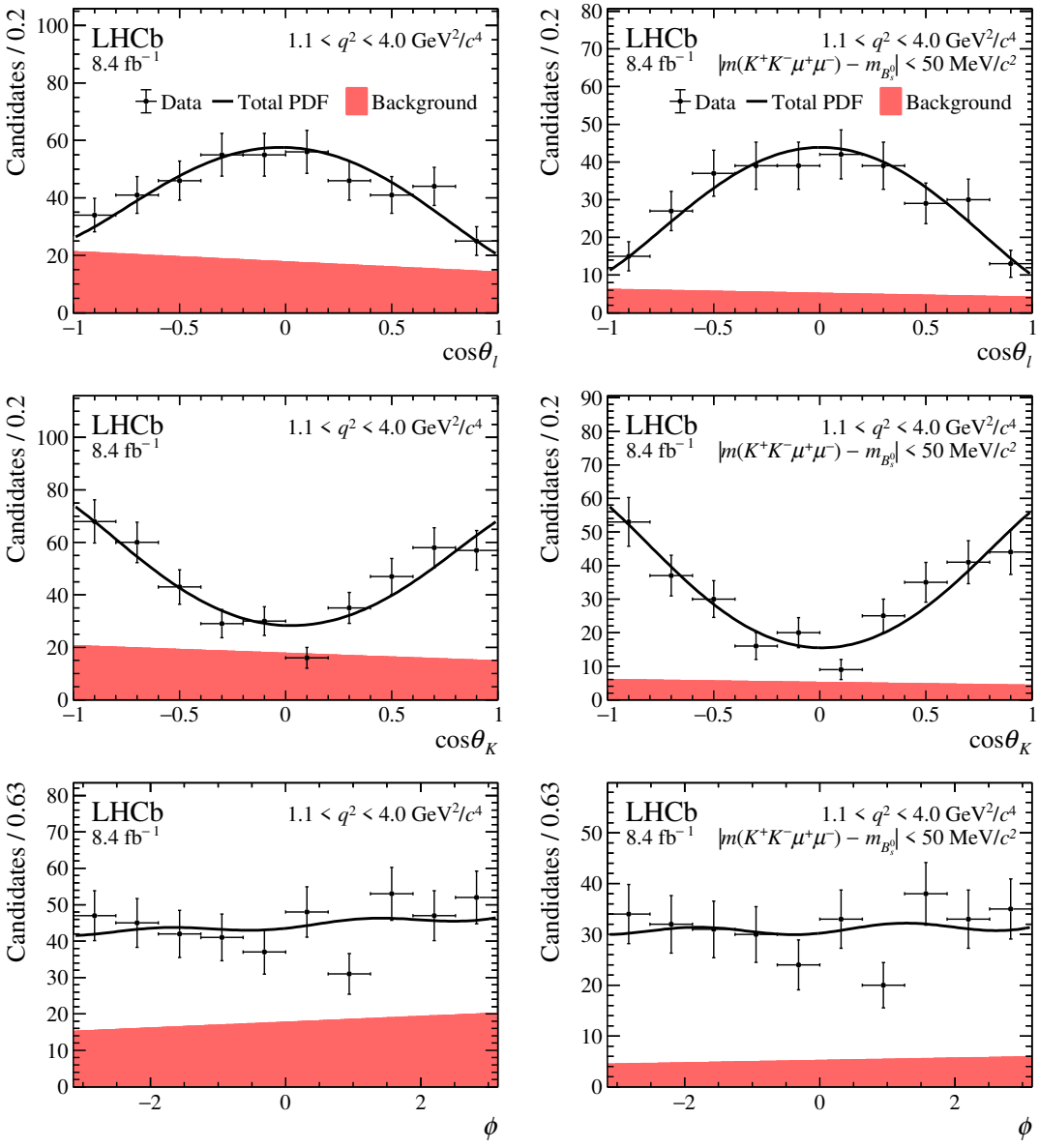

Figure 6: Projections in the region $1.1 < q^2 < 4.0\,\mathrm{GeV}^2/c^4$ for the angular distributions of the combined 2011–2012, 2016 and 2017–2018 data set. The data are overlaid with the projection of the combined PDF. The red shaded area indicates the background component and the solid black line the total PDF. The angular projections are given for candidates in (left) the entire mass region used to determine the observables in this paper and (right) the signal mass window $\pm 50\,\mathrm{MeV}/c^2$ around the known B_s^0 mass.

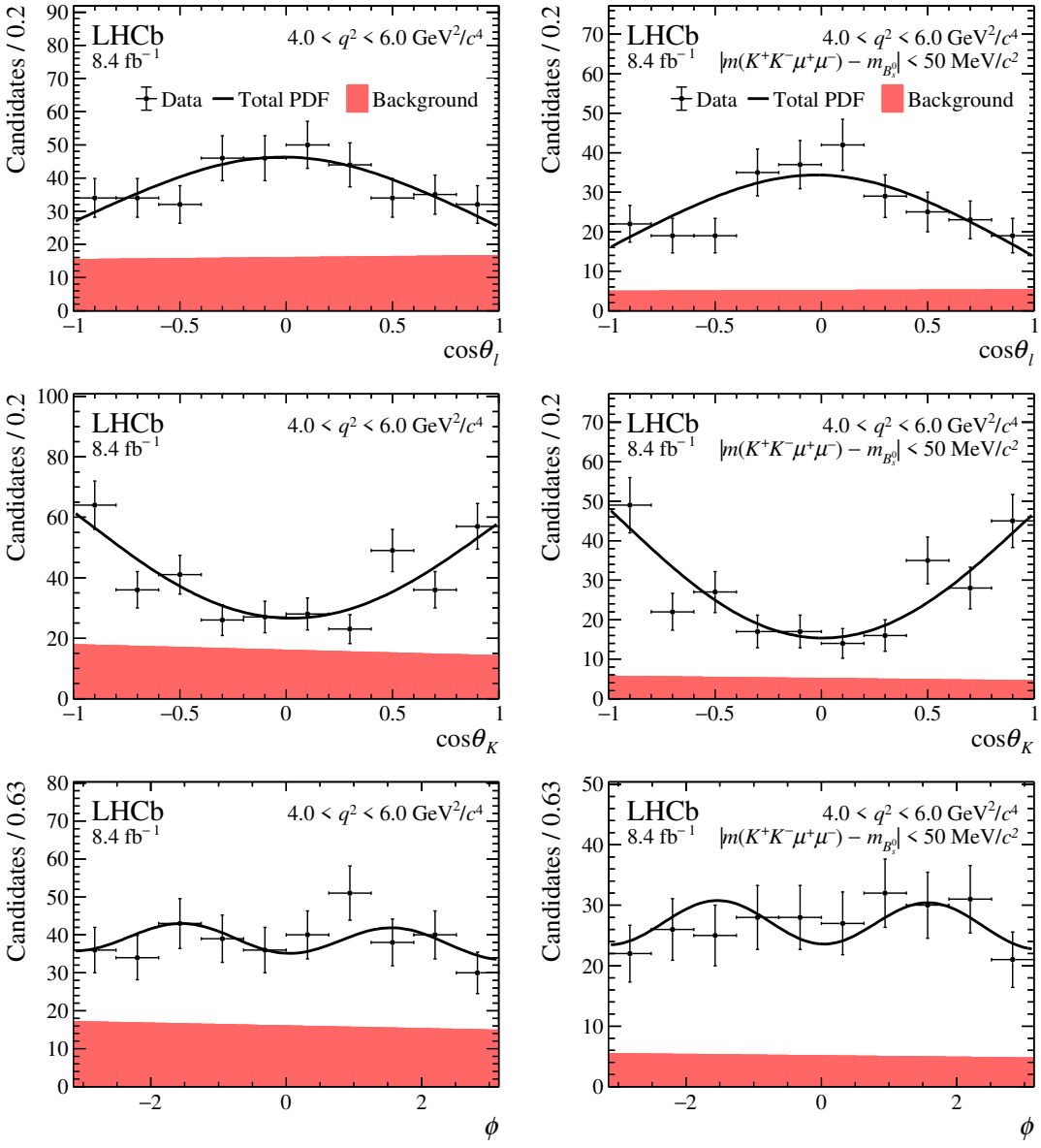

Figure 7: Projections in the region $4.0 < q^2 < 6.0\,\mathrm{GeV}^2/c^4$ for the angular distributions of the combined 2011–2012, 2016 and 2017–2018 data sets. The data are overlaid with the projection of the combined PDF. The red shaded area indicates the background component and the solid black line the total PDF. The angular projections are given for candidates in (left) the entire mass region used to determine the observables in this paper and (right) the signal mass window $\pm 50\,\mathrm{MeV}/c^2$ around the known B_s^0 mass.

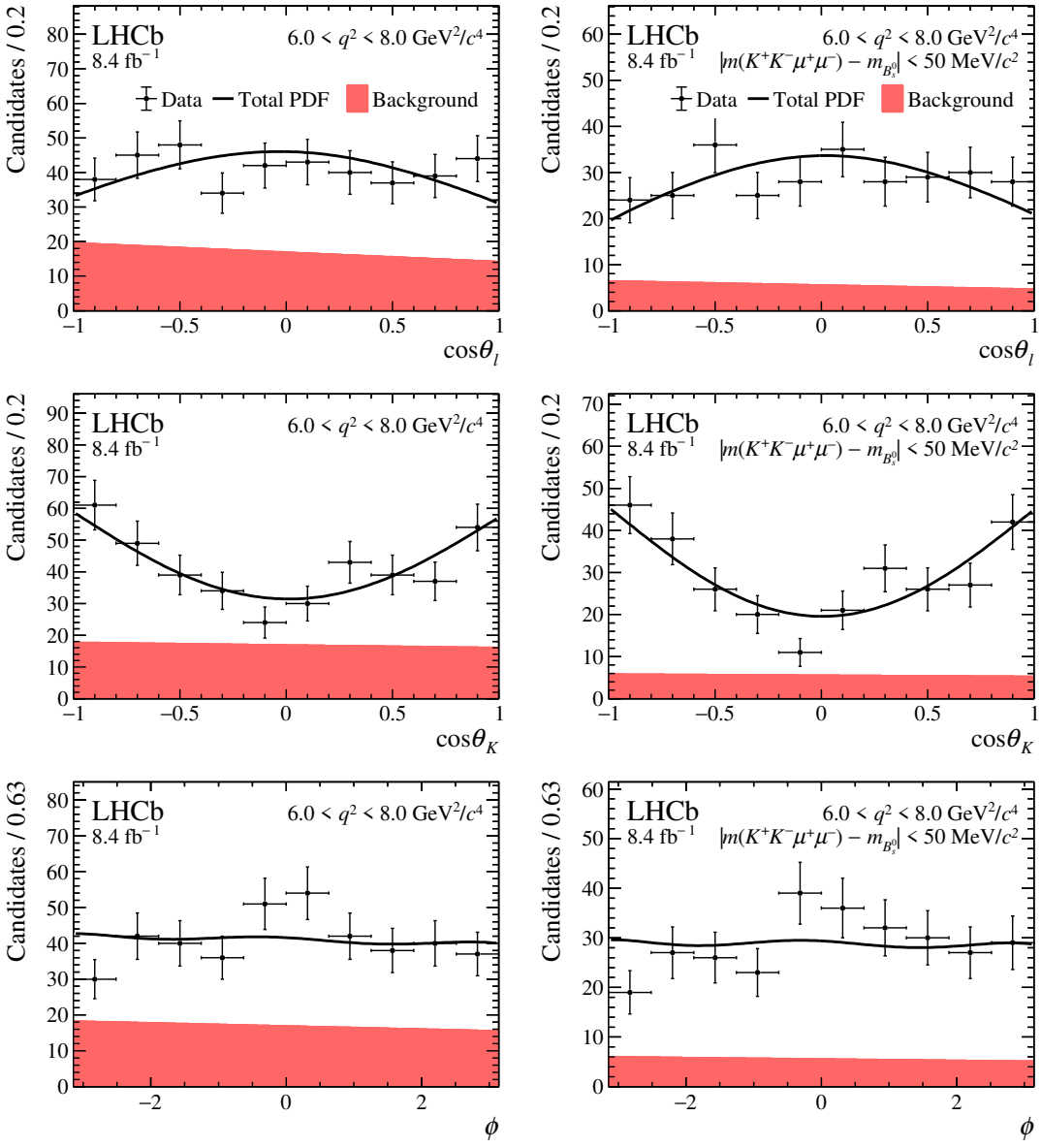

Figure 8: Projections in the region $6.0 < q^2 < 8.0\,\mathrm{GeV}^2/c^4$ for the angular distributions of the combined 2011–2012, 2016 and 2017–2018 data sets. The data are overlaid with the projection of the combined PDF. The red shaded area indicates the background component and the solid black line the total PDF. The angular projections are given for candidates in (left) the entire mass region used to determine the observables in this paper and (right) the signal mass window $\pm 50\,\mathrm{MeV}/c^2$ around the known B_s^0 mass.

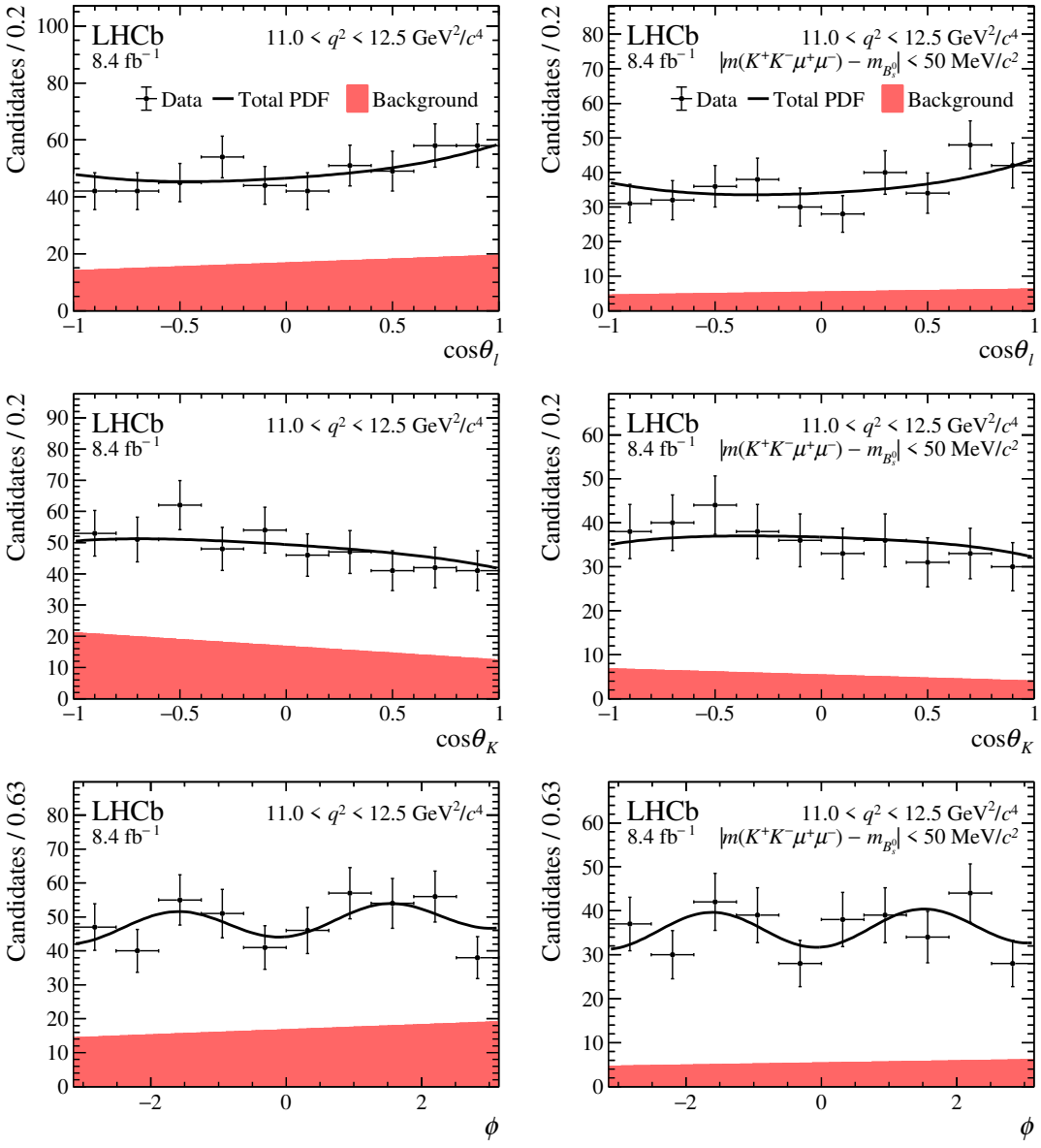

Figure 9: Projections in the region $11.0 < q^2 < 12.5\,\text{GeV}^2/c^4$ for the angular distributions of the combined 2011–2012, 2016 and 2017–2018 data sets. The data are overlaid with the projection of the combined PDF. The red shaded area indicates the background component and the solid black line the total PDF. The angular projections are given for candidates in (left) the entire mass region used to determine the observables in this paper and (right) the signal mass window $\pm 50\,\text{MeV}/c^2$ around the known B_s^0 mass.

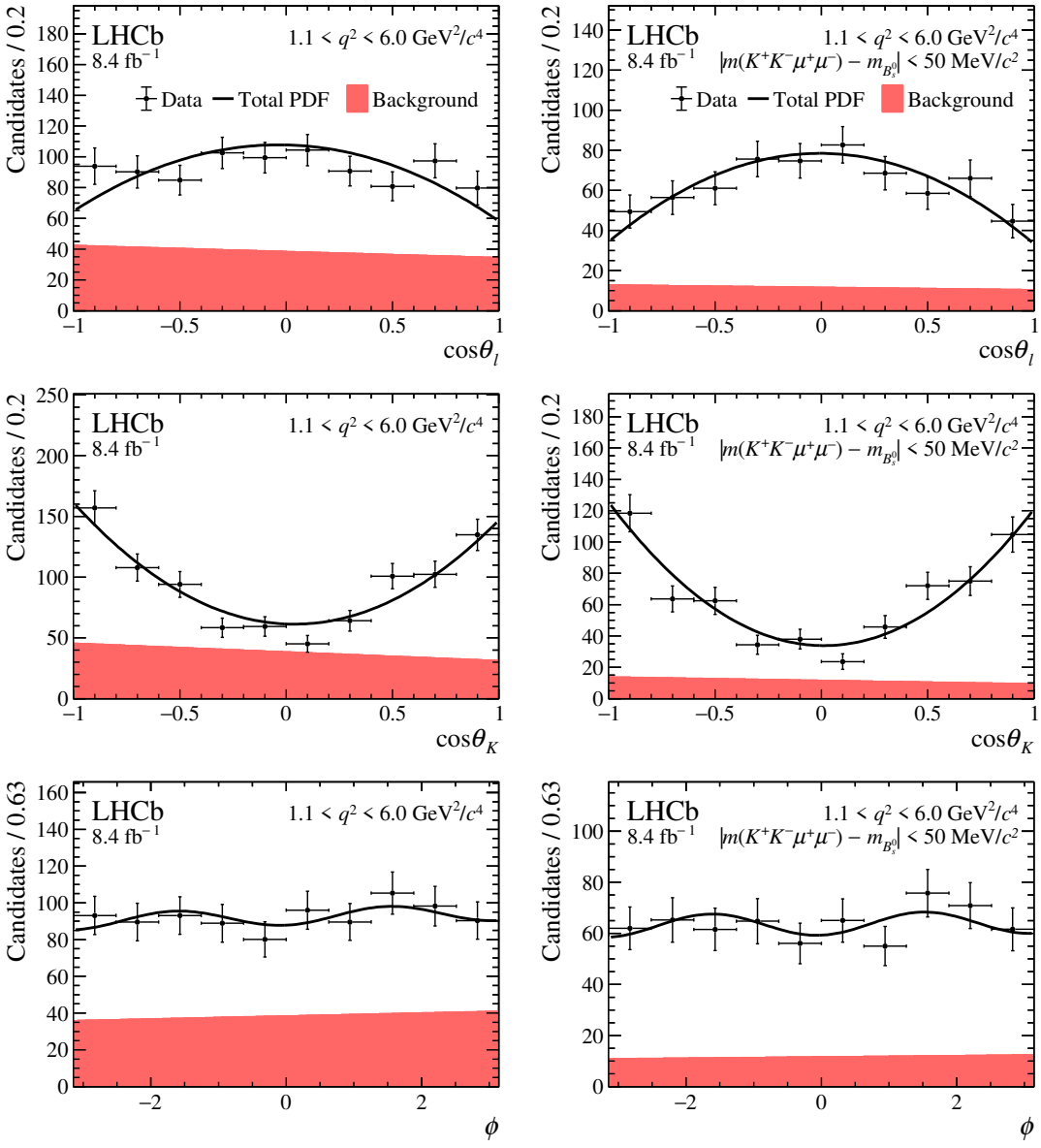

Figure 10: Projections in the region $1.1 < q^2 < 6.0\,\text{GeV}^2/c^4$ for the angular distributions of the combined 2011–2012, 2016 and 2017–2018 data sets. The data are overlaid with the projection of the combined PDF. The red shaded area indicates the background component and the solid black line the total PDF. The angular projections are given for candidates in (left) the entire mass region used to determine the observables in this paper and (right) the signal mass window $\pm 50\,\text{MeV}/c^2$ around the known B_s^0 mass.

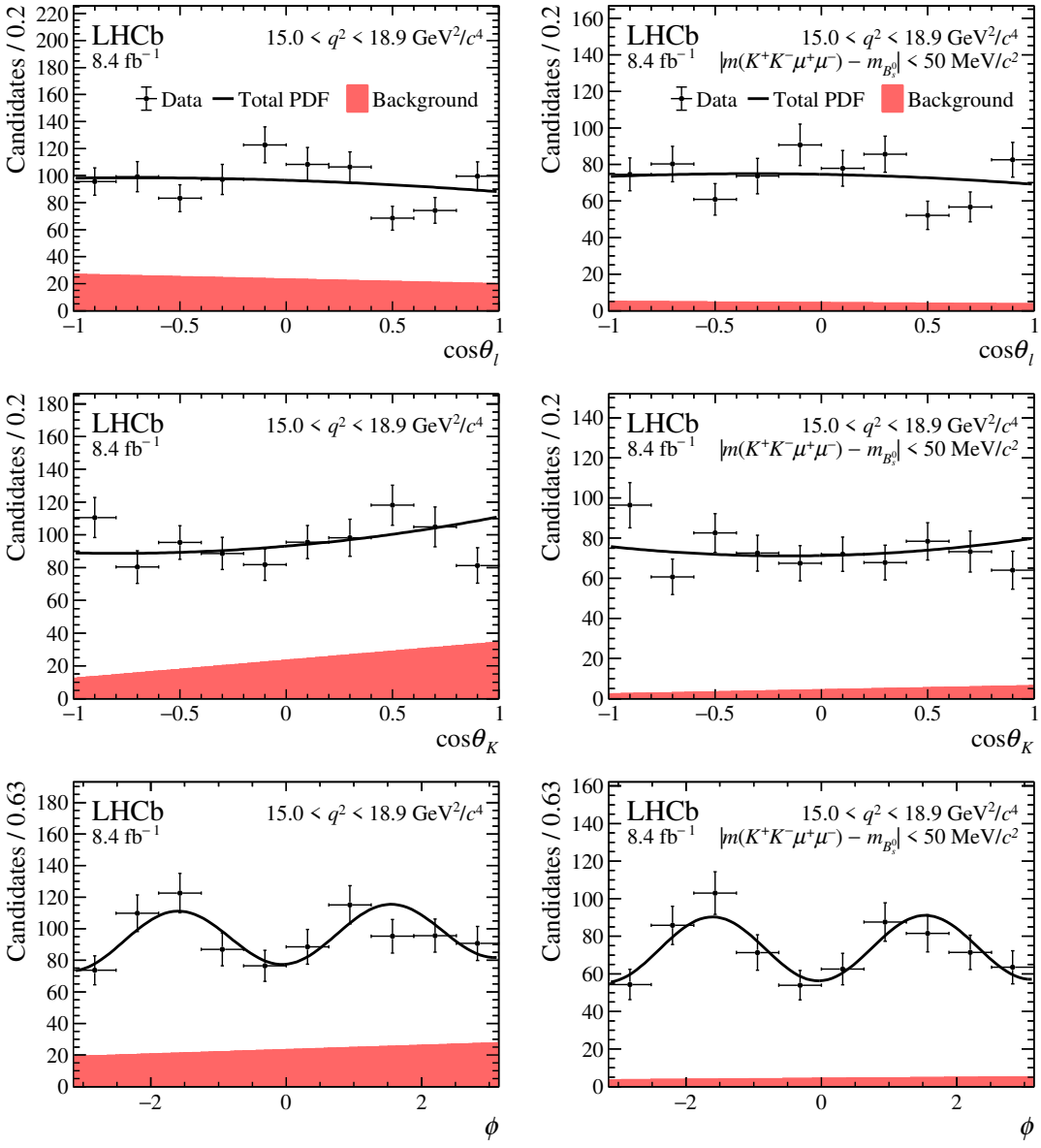

Figure 11: Projections in the region $15.0 < q^2 < 18.9\,\text{GeV}^2/c^4$ for the angular distributions of the combined 2011–2012, 2016 and 2017–2018 data sets. The data are overlaid with the projection of the combined PDF. The red shaded area indicates the background component and the solid black line the total PDF. The angular projections are given for candidates in (left) the entire mass region used to determine the observables in this paper and (right) the signal mass window $\pm 50\,\text{MeV}/c^2$ around the known B_s^0 mass.

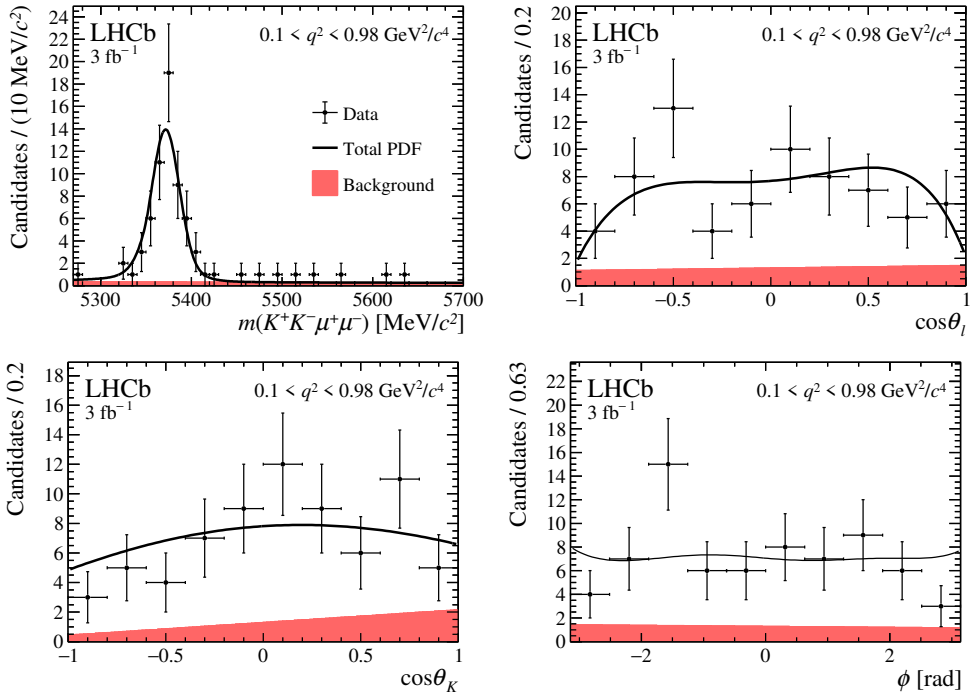

Figure 12: Mass and angular distributions of $B_s^0 \to \phi\mu^+\mu^-$ candidates in the region $0.1 < q^2 < 0.98\,\text{GeV}^2/c^4$ for data taken in 2011–2012. The data are overlaid with the projections of the fitted PDF.

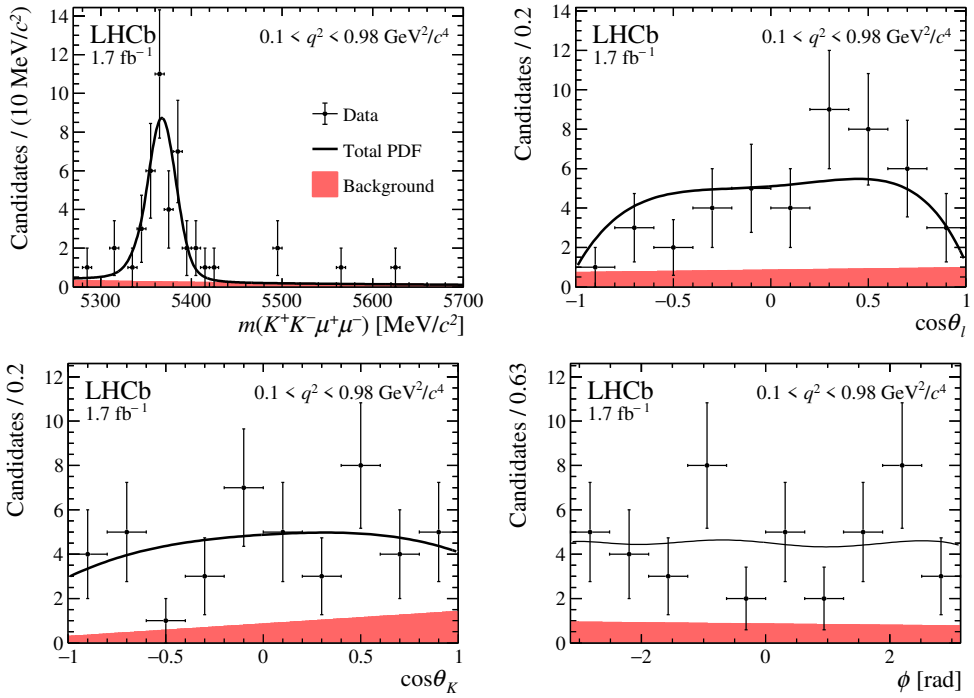

Figure 13: Mass and angular distributions of $B_s^0 \to \phi\mu^+\mu^-$ candidates in the region $0.1 < q^2 < 0.98\,\text{GeV}^2/c^4$ for data taken in 2016. The data are overlaid with the projections of the fitted PDF.

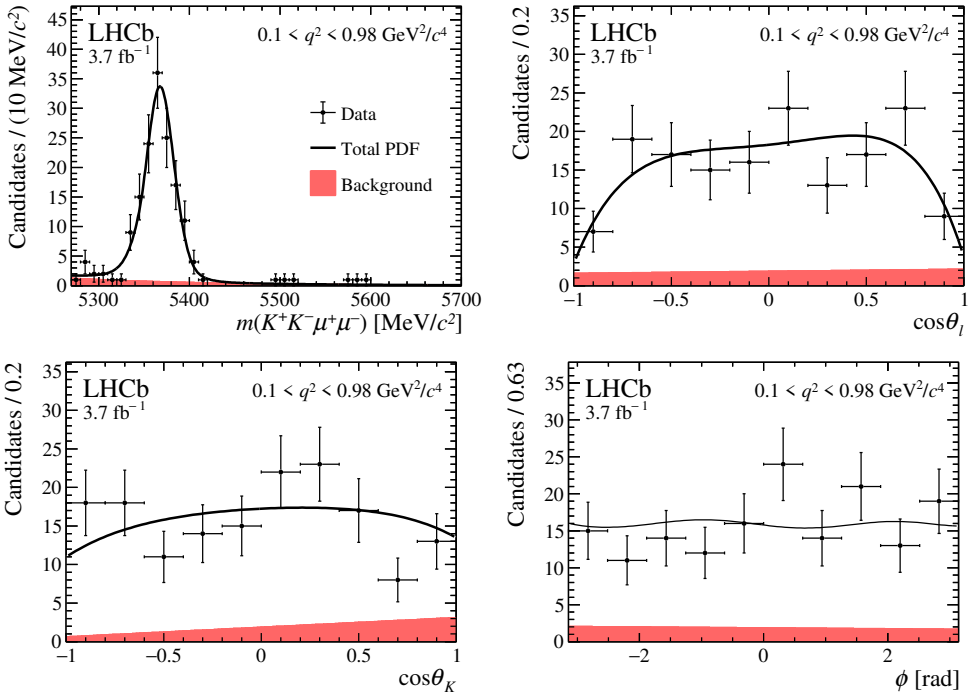

Figure 14: Mass and angular distributions of $B_s^0 \to \phi\mu^+\mu^-$ candidates in the region $0.1 < q^2 < 0.98\,\text{GeV}^2/c^4$ for data taken in 2017–2018. The data are overlaid with the projections of the fitted PDF.

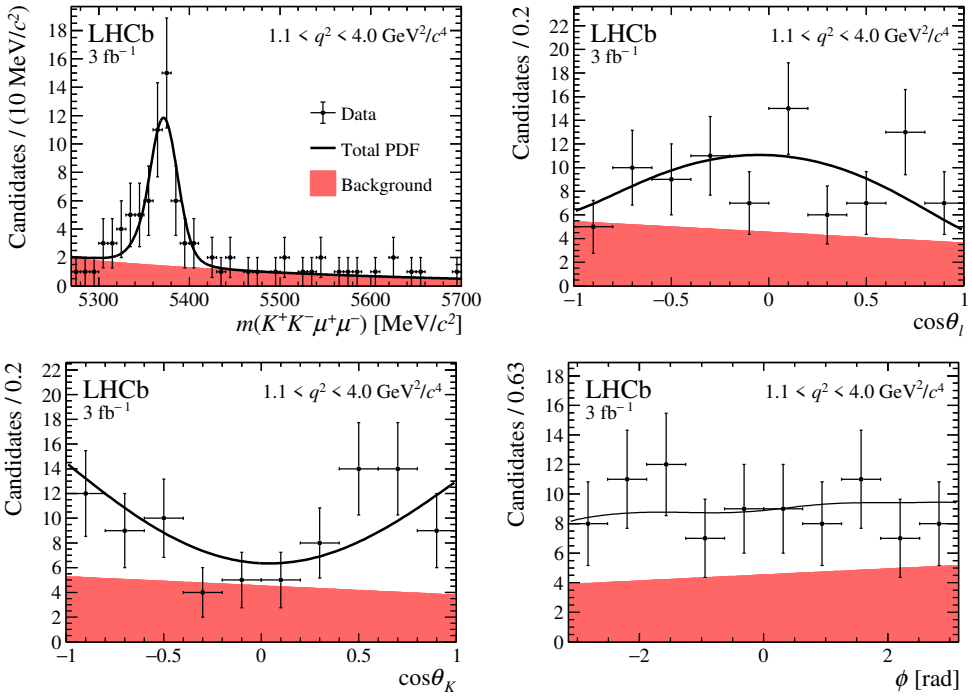

Figure 15: Mass and angular distributions of $B_s^0 \to \phi\mu^+\mu^-$ candidates in the region $1.1 < q^2 < 4.0\,\text{GeV}^2/c^4$ for data taken in 2011–2012. The data are overlaid with the projections of the fitted PDF.

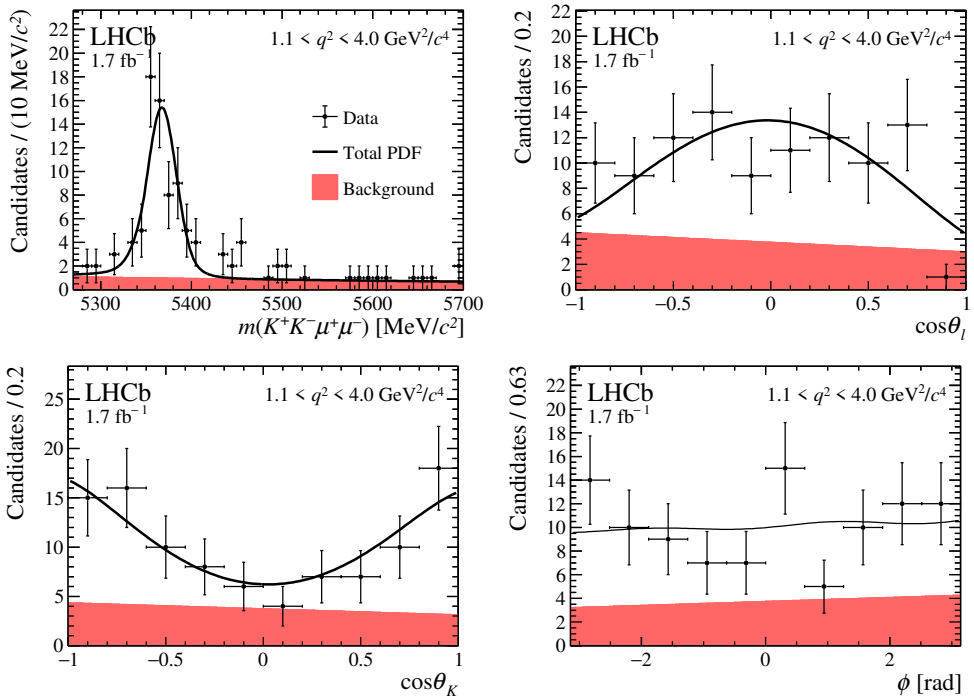

Figure 16: Mass and angular distributions of $B_s^0 \to \phi\mu^+\mu^-$ candidates in the region $1.1 < q^2 < 4.0\,\mathrm{GeV}^2/c^4$ for data taken in 2016. The data are overlaid with the projections of the fitted PDF.

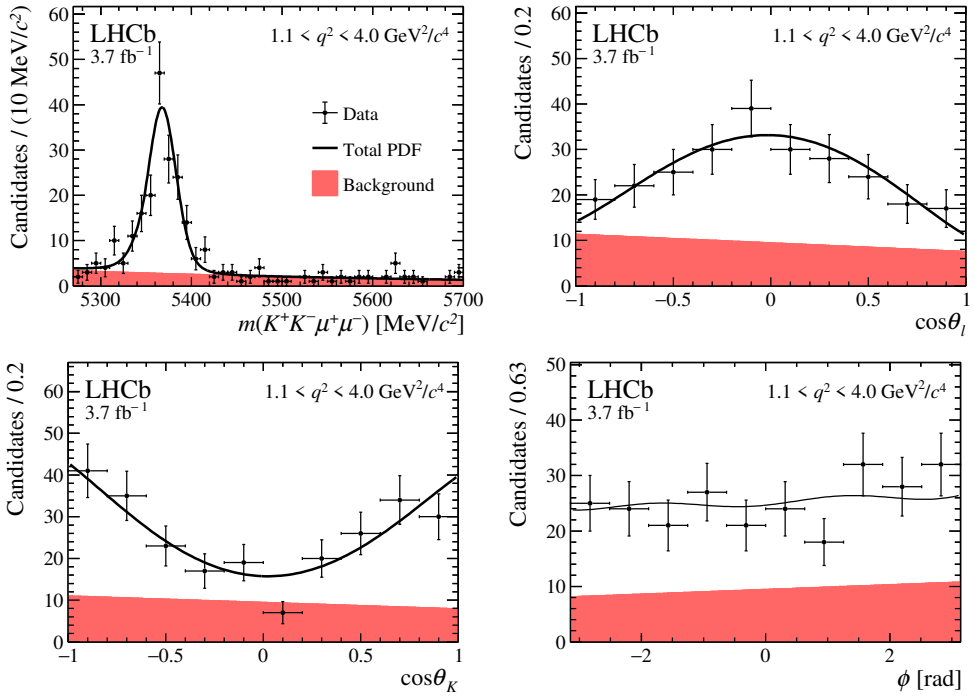

Figure 17: Mass and angular distributions of $B_s^0 \to \phi\mu^+\mu^-$ candidates in the region $1.1 < q^2 < 4.0\,\mathrm{GeV}^2/c^4$ for data taken in 2017–2018. The data are overlaid with the projections of the fitted PDF.

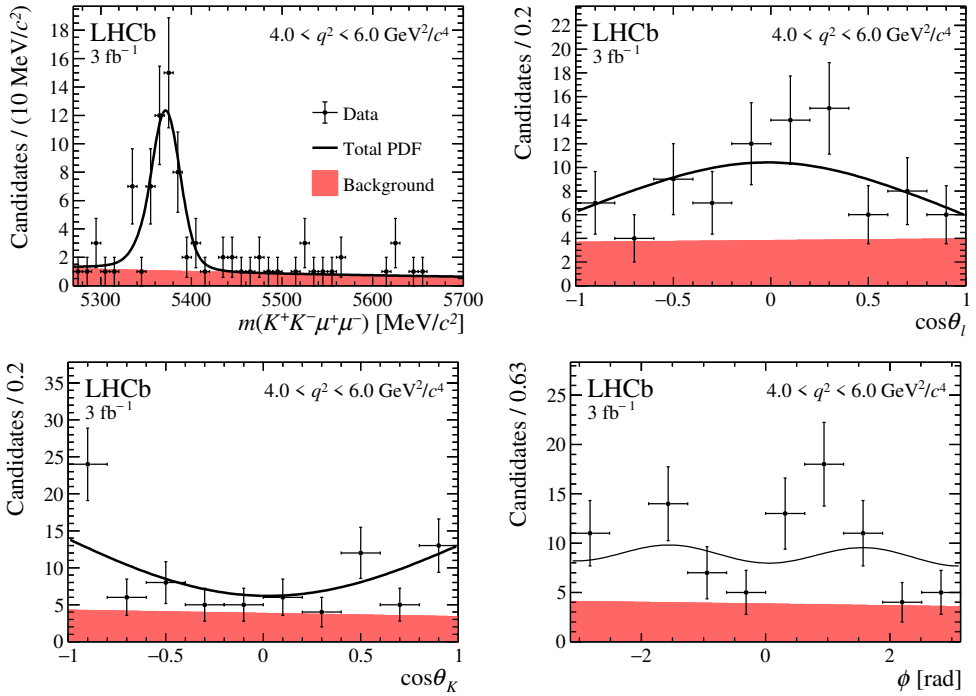

Figure 18: Mass and angular distributions of $B_s^0 \to \phi\mu^+\mu^-$ candidates in the region $4.0 < q^2 < 6.0\,\mathrm{GeV}^2/c^4$ for data taken in 2011–2012. The data are overlaid with the projections of the fitted PDF.

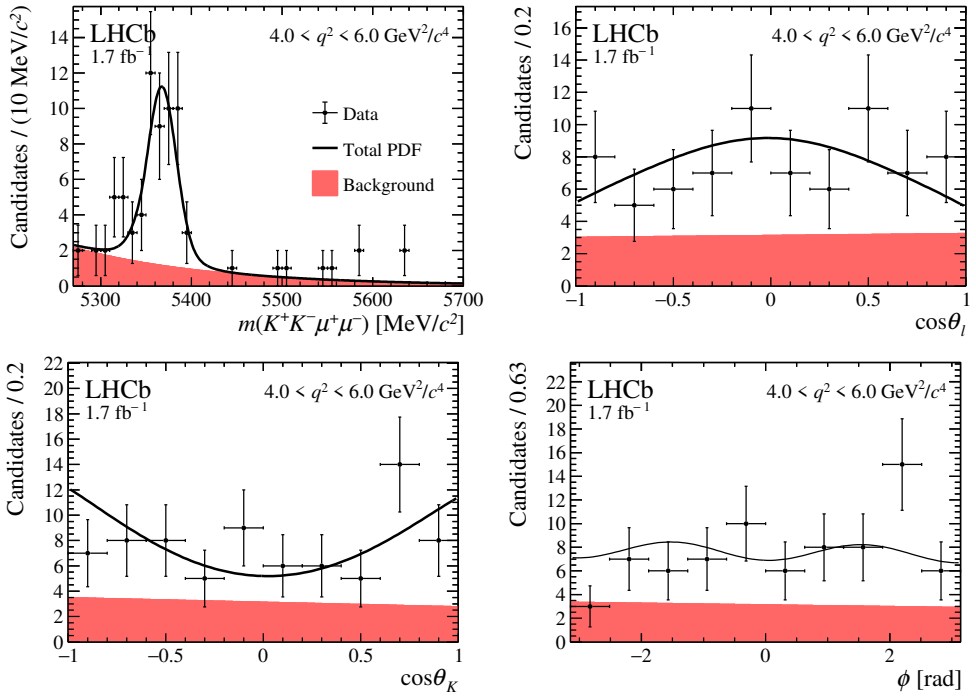

Figure 19: Mass and angular distributions of $B_s^0 \to \phi\mu^+\mu^-$ candidates in the region $4.0 < q^2 < 6.0\,\mathrm{GeV}^2/c^4$ for data taken in 2016. The data are overlaid with the projections of the fitted PDF.

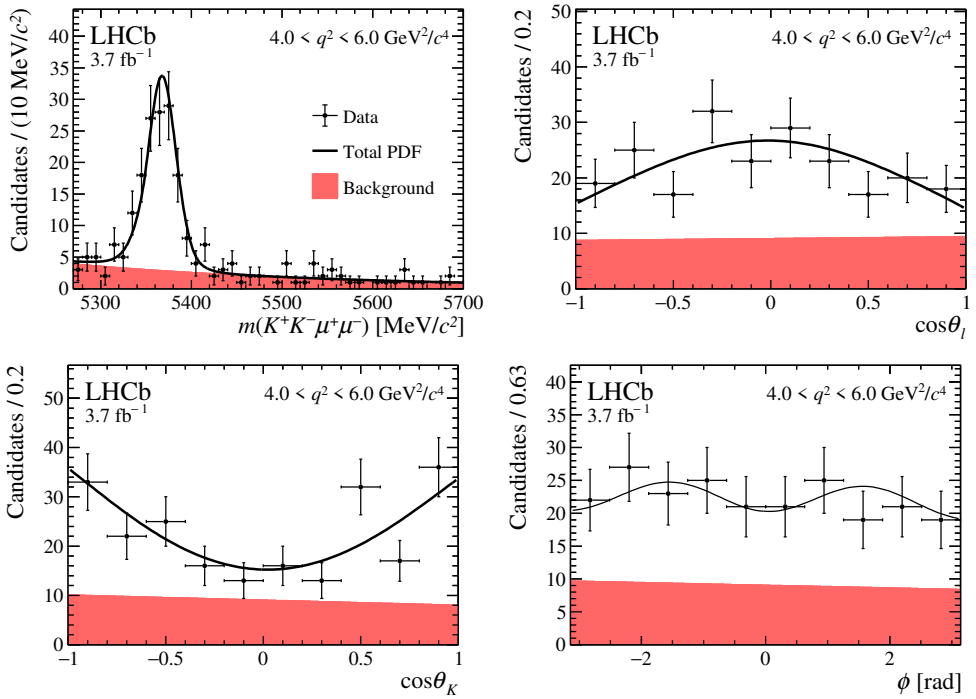

Figure 20: Mass and angular distributions of $B_s^0 \to \phi\mu^+\mu^-$ candidates in the region $4.0 < q^2 < 6.0\,\mathrm{GeV}^2/c^4$ for data taken in 2017–2018. The data are overlaid with the projections of the fitted PDF.

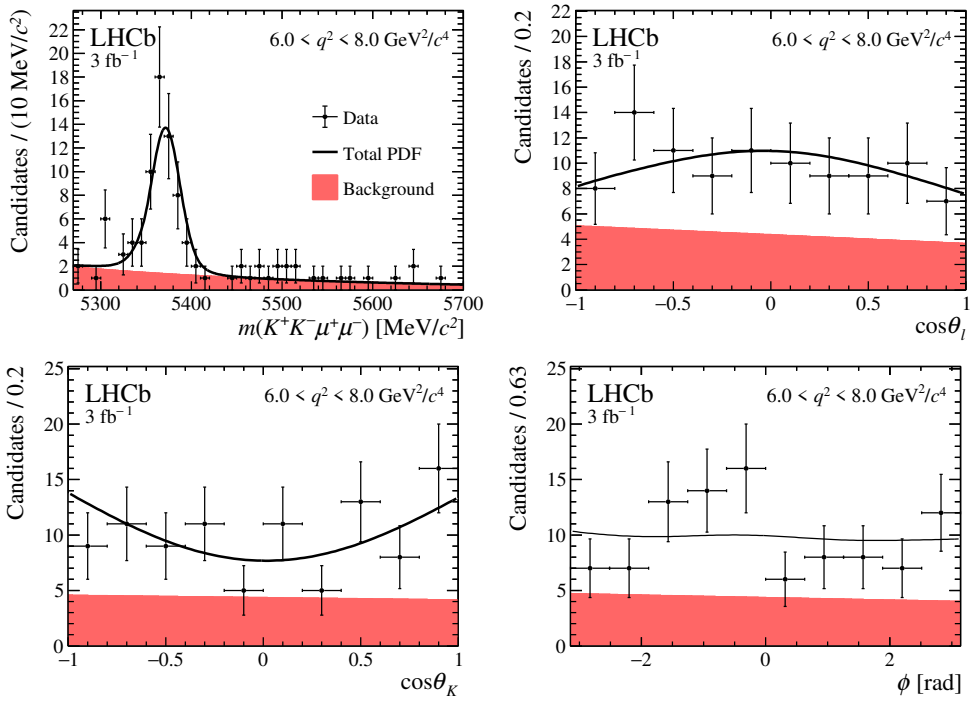

Figure 21: Mass and angular distributions of $B_s^0 \to \phi\mu^+\mu^-$ candidates in the region $6.0 < q^2 < 8.0\,\mathrm{GeV}^2/c^4$ for data taken in 2011–2012. The data are overlaid with the projections of the fitted PDF.

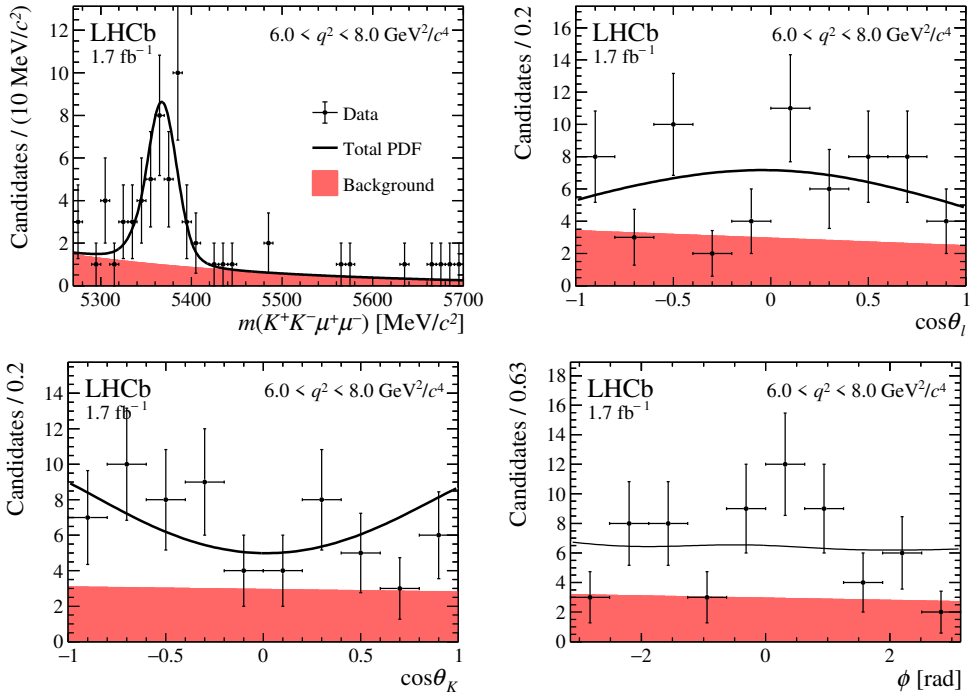

Figure 22: Mass and angular distributions of $B_s^0 \to \phi\mu^+\mu^-$ candidates in the region $6.0 < q^2 < 8.0\,\text{GeV}^2/c^4$ for data taken in 2016. The data are overlaid with the projections of the fitted PDF.

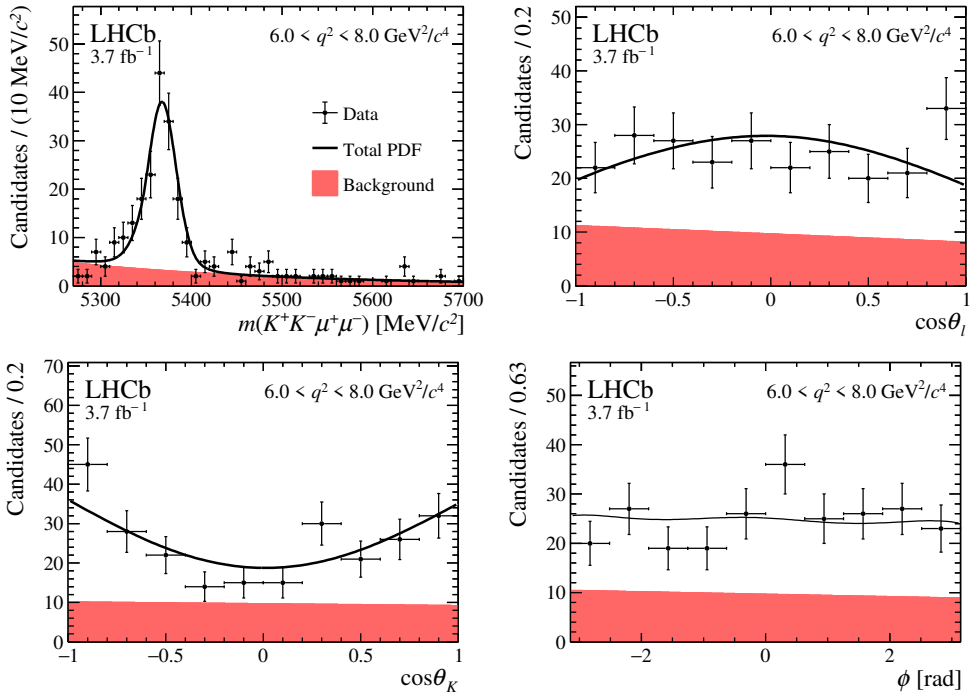

Figure 23: Mass and angular distributions of $B_s^0 \to \phi\mu^+\mu^-$ candidates in the region $6.0 < q^2 < 8.0\,\text{GeV}^2/c^4$ for data taken in 2017–2018. The data are overlaid with the projections of the fitted PDF.

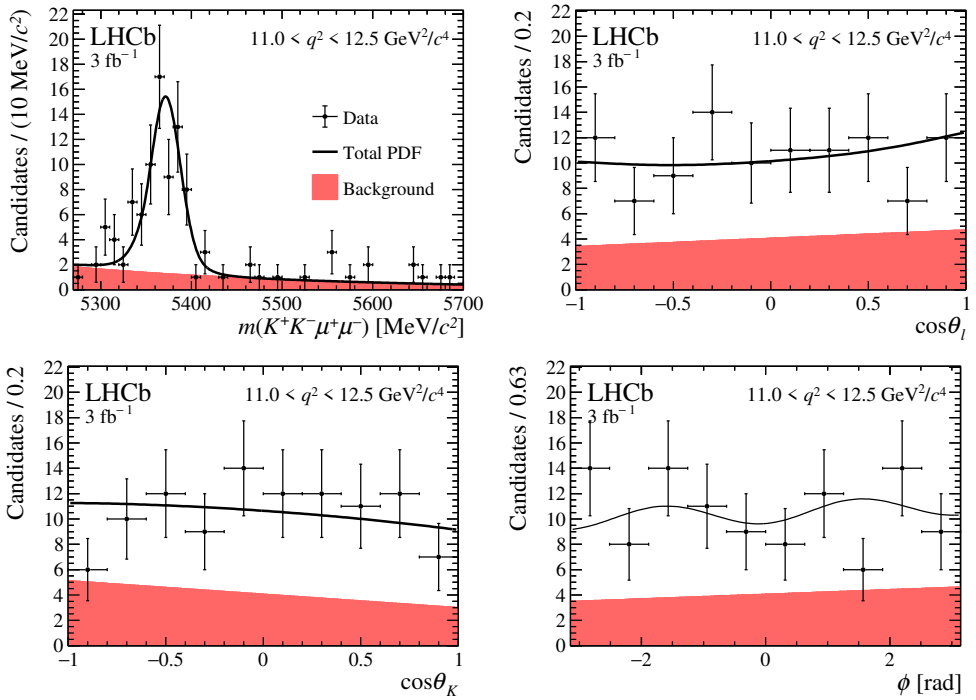

Figure 24: Mass and angular distributions of $B_s^0 \to \phi\mu^+\mu^-$ candidates in the region $11.0 < q^2 < 12.5\,\mathrm{GeV}^2/c^4$ for data taken in 2011–2012. The data are overlaid with the projections of the fitted PDF.

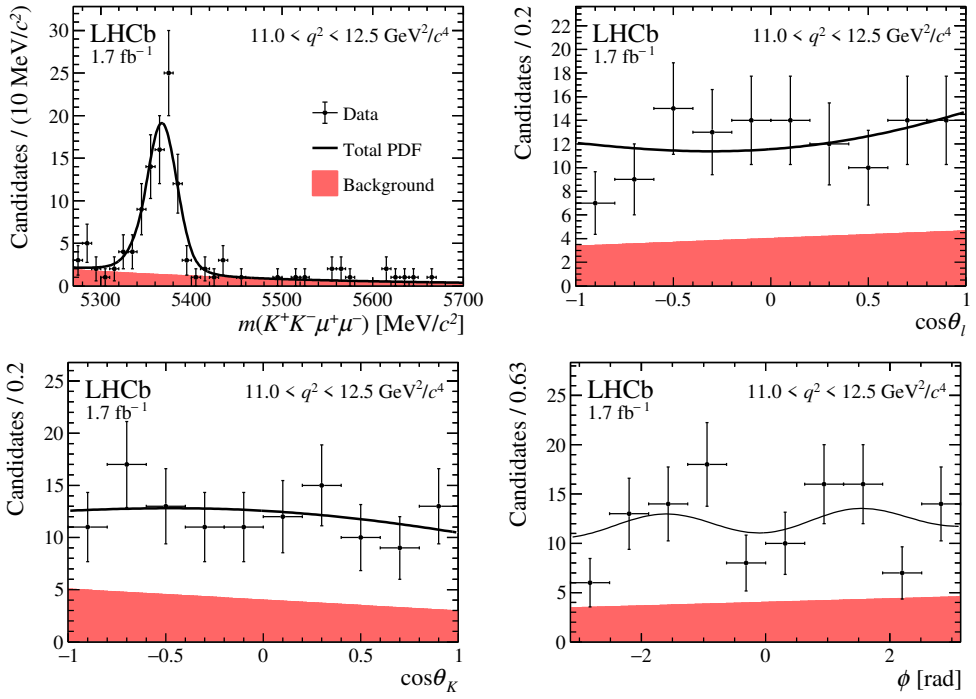

Figure 25: Mass and angular distributions of $B_s^0 \to \phi\mu^+\mu^-$ candidates in the region $11.0 < q^2 < 12.5\,\mathrm{GeV}^2/c^4$ for data taken in 2016. The data are overlaid with the projections of the fitted PDF.

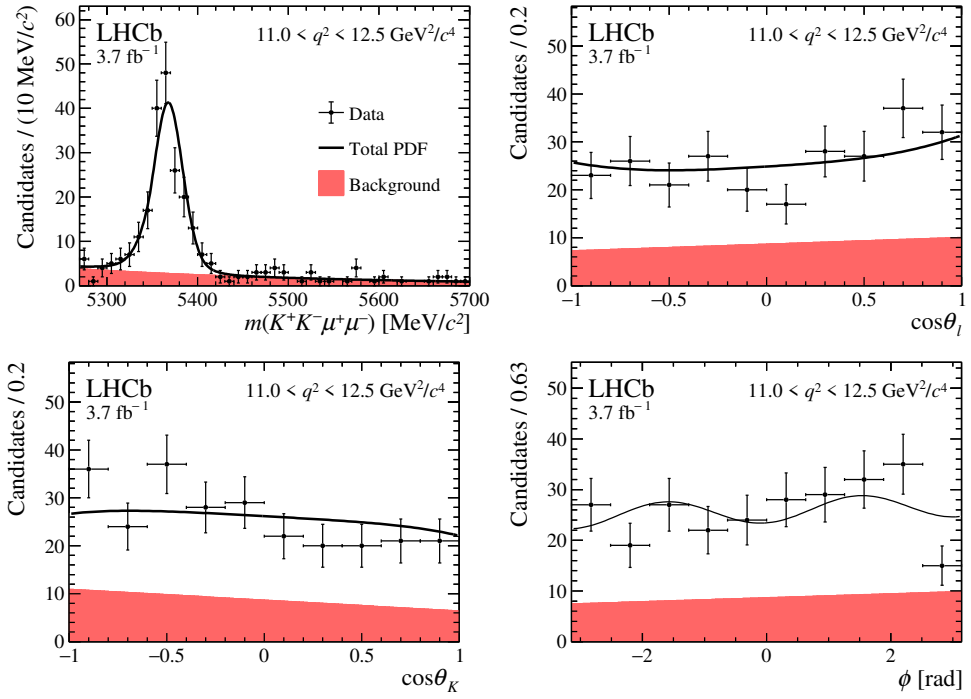

Figure 26: Mass and angular distributions of $B_s^0 \to \phi\mu^+\mu^-$ candidates in the region $11.0 < q^2 < 12.5\,\mathrm{GeV}^2/c^4$ for data taken in 2017–2018. The data are overlaid with the projections of the fitted PDF.

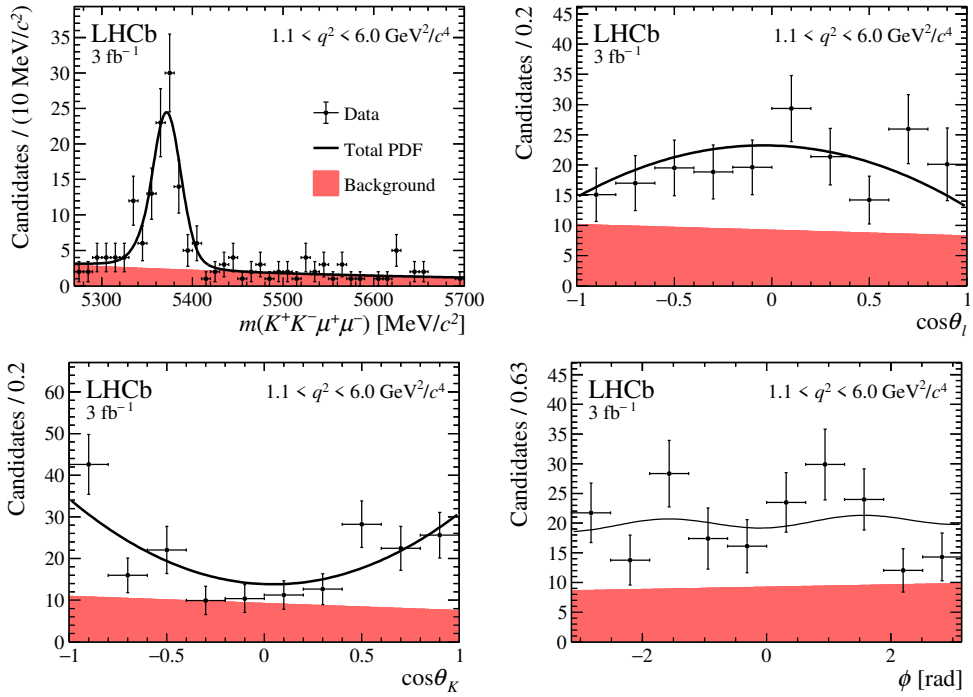

Figure 27: Mass and angular distributions of $B_s^0 \to \phi\mu^+\mu^-$ candidates in the region $1.1 < q^2 < 6.0\,\mathrm{GeV}^2/c^4$ for data taken in 2011–2012. The data are overlaid with the projections of the fitted PDF.

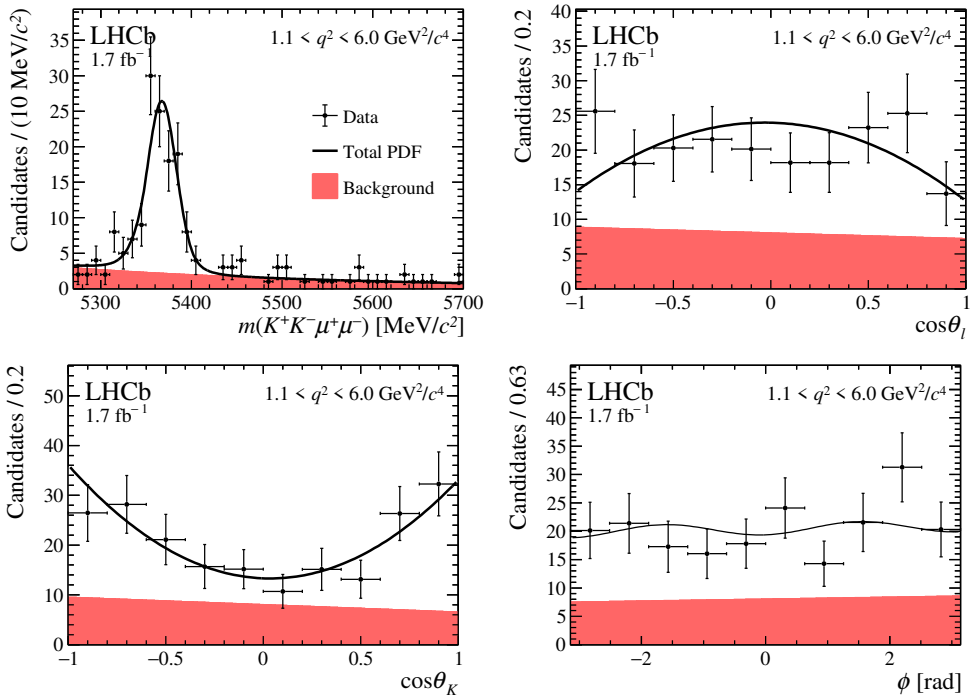

Figure 28: Mass and angular distributions of $B_s^0 \to \phi\mu^+\mu^-$ candidates in the region $1.1 < q^2 < 6.0\,\mathrm{GeV}^2/c^4$ for data taken in 2016. The data are overlaid with the projections of the fitted PDF.

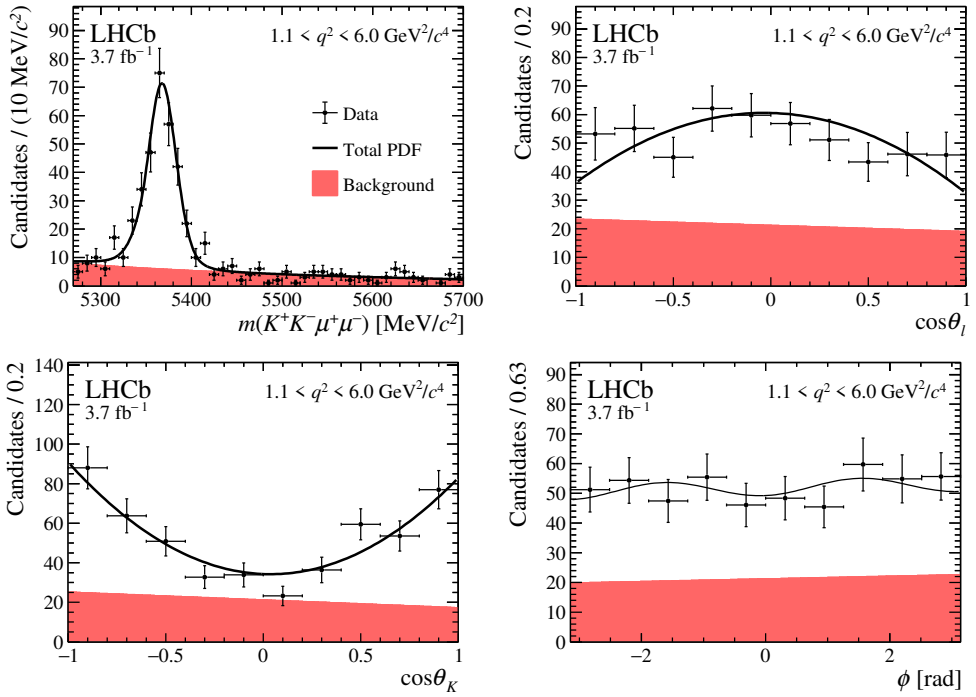

Figure 29: Mass and angular distributions of $B_s^0 \to \phi\mu^+\mu^-$ candidates in the region $1.1 < q^2 < 6.0\,\mathrm{GeV}^2/c^4$ for data taken in 2017–2018. The data are overlaid with the projections of the fitted PDF.

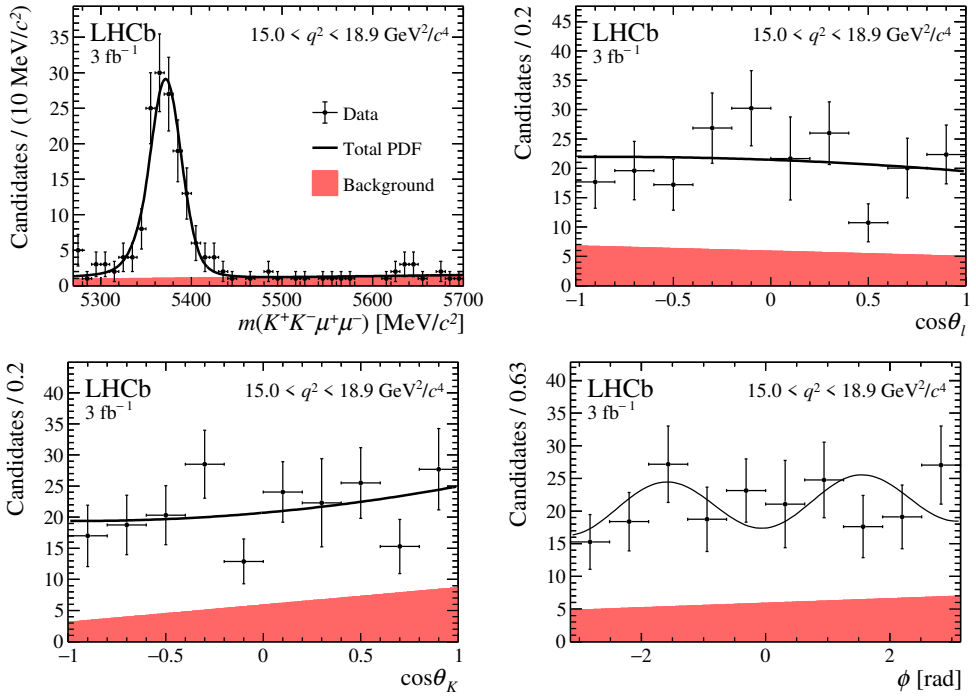

Figure 30: Mass and angular distributions of $B_s^0 \to \phi\mu^+\mu^-$ candidates in the region $15.0 < q^2 < 18.9\,\mathrm{GeV}^2/c^4$ for data taken in 2011–2012. The data are overlaid with the projections of the fitted PDF.

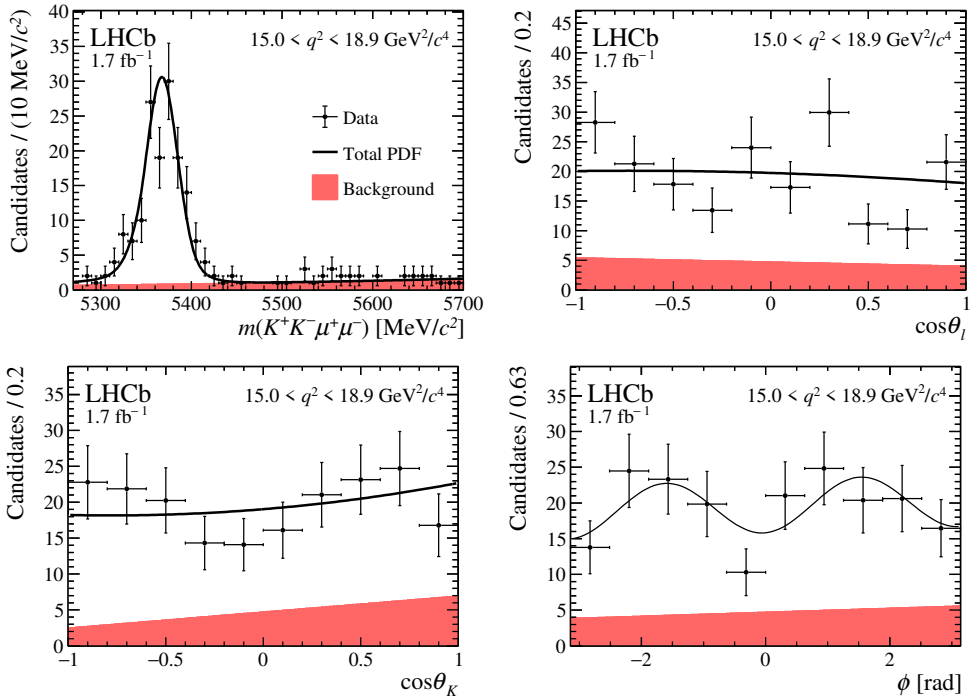

Figure 31: Mass and angular distributions of $B_s^0 \to \phi\mu^+\mu^-$ candidates in the region $15.0 < q^2 < 18.9\,\mathrm{GeV}^2/c^4$ for data taken in 2016. The data are overlaid with the projections of the fitted PDF.

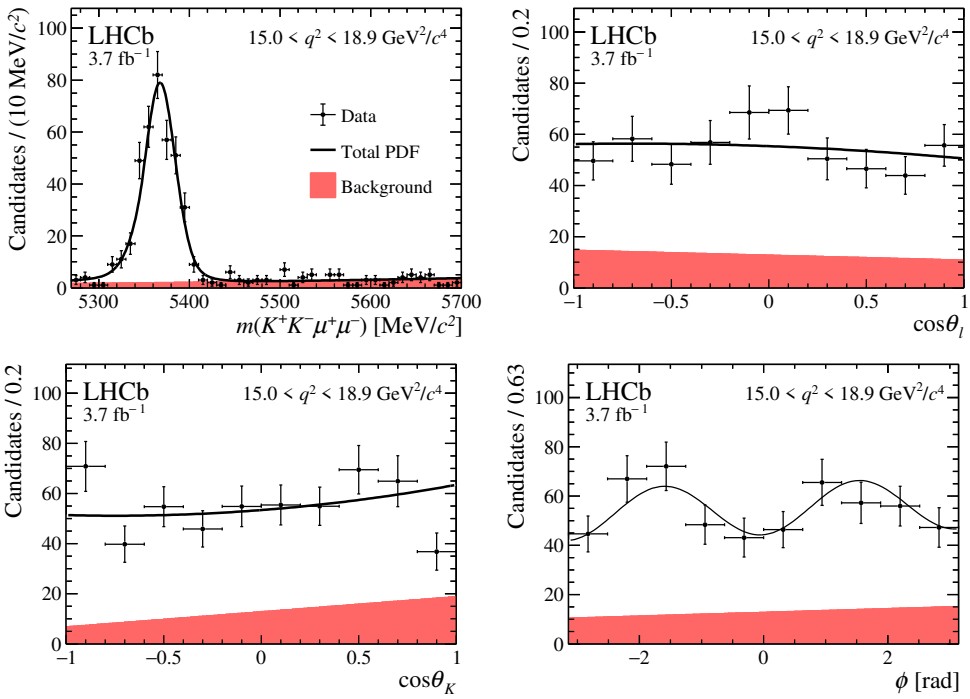

Figure 32: Mass and angular distributions of $B_s^0 \to \phi\mu^+\mu^-$ candidates in the region $15.0 < q^2 < 18.9\,\mathrm{GeV}^2/c^4$ for data taken in 2017–2018. The data are overlaid with the projections of the fitted PDF.

B Correlation matrices

The linear correlations obtained from the fit of the angular observables are given in Tables 3–5.

Table 3: Correlation matrix for the q^2 regions $0.1 < q^2 < 0.98\,\mathrm{GeV}^2/c^4$ and $1.1 < q^2 < 4.0\,\mathrm{GeV}^2/c^4$.

Correlation matrix for $0.1 < q^2 < 0.98\,\mathrm{GeV}^2/c^4$								
	F_L	S_3	S_4	A_5	A_FB^{CP}	S_7	A_8	A_9
F_L	1.00	−0.03	0.06	0.10	0.02	−0.20	−0.05	−0.04
S_3		1.00	0.11	0.00	−0.06	0.07	−0.05	0.02
S_4			1.00	0.03	−0.06	0.08	−0.05	−0.01
A_5				1.00	0.12	−0.07	0.06	−0.09
A_FB^{CP}					1.00	0.02	−0.04	0.07
S_7						1.00	0.29	−0.03
A_8							1.00	0.06
A_9								1.00

Correlation matrix for $1.1 < q^2 < 4.0\,\mathrm{GeV}^2/c^4$								
	F_L	S_3	S_4	A_5	A_FB^{CP}	S_7	A_8	A_9
F_L	1.00	−0.12	0.03	−0.03	−0.07	−0.12	0.03	−0.01
S_3		1.00	−0.07	−0.00	0.03	0.04	−0.04	0.05
S_4			1.00	0.02	0.09	0.01	−0.02	−0.02
A_5				1.00	−0.08	0.02	0.01	0.06
A_FB^{CP}					1.00	0.02	−0.02	0.03
S_7						1.00	−0.06	0.06
A_8							1.00	−0.04
A_9								1.00

Table 4: Correlation matrix for the q^2 regions $4.0 < q^2 < 6.0\,\mathrm{GeV}^2/c^4$, $6.0 < q^2 < 8.0\,\mathrm{GeV}^2/c^4$ and $11.0 < q^2 < 12.5\,\mathrm{GeV}^2/c^4$.

Correlation matrix for $4.0 < q^2 < 6.0\,\mathrm{GeV}^2/c^4$								
	F_L	S_3	S_4	A_5	A_FB^{CP}	S_7	A_8	A_9
F_L	1.00	0.15	0.06	−0.08	0.01	−0.01	−0.04	−0.08
S_3		1.00	−0.04	−0.02	0.05	−0.06	−0.04	0.22
S_4			1.00	−0.12	−0.02	0.05	−0.04	−0.07
A_5				1.00	−0.11	−0.06	0.04	0.05
A_FB^{CP}					1.00	−0.01	0.10	0.01
S_7						1.00	−0.13	0.02
A_8							1.00	−0.05
A_9								1.00

Correlation matrix for $6.0 < q^2 < 8.0\,\mathrm{GeV}^2/c^4$								
	F_L	S_3	S_4	A_5	A_FB^{CP}	S_7	A_8	A_9
F_L	1.00	0.03	0.07	−0.04	−0.10	0.01	−0.03	−0.04
S_3		1.00	−0.08	−0.02	−0.02	−0.01	0.04	−0.05
S_4			1.00	−0.09	0.02	−0.05	−0.08	−0.06
A_5				1.00	−0.12	−0.05	−0.05	0.05
A_FB^{CP}					1.00	−0.04	−0.04	−0.01
S_7						1.00	−0.14	0.03
A_8							1.00	−0.05
A_9								1.00

Correlation matrix for $11.0 < q^2 < 12.5\,\mathrm{GeV}^2/c^4$								
	F_L	S_3	S_4	A_5	A_FB^{CP}	S_7	A_8	A_9
F_L	1.00	0.09	0.02	−0.05	−0.10	−0.03	−0.04	−0.07
S_3		1.00	−0.14	−0.01	−0.02	0.11	−0.06	−0.06
S_4			1.00	−0.04	0.18	−0.01	−0.07	−0.05
A_5				1.00	−0.23	−0.11	0.01	−0.02
A_FB^{CP}					1.00	0.04	−0.06	0.02
S_7						1.00	0.06	−0.05
A_8							1.00	−0.11
A_9								1.00

Table 5: Correlation matrix for the q^2 region $1.1 < q^2 < 6.0\,\mathrm{GeV}^2/c^4$ and $15.0 < q^2 < 18.9\,\mathrm{GeV}^2/c^4$.

Correlation matrix for $1.1 < q^2 < 6.0\,\mathrm{GeV}^2/c^4$								
	F_L	S_3	S_4	A_5	A_FB^{CP}	S_7	A_8	A_9
F_L	1.00	−0.03	0.05	−0.02	−0.07	−0.08	−0.04	−0.03
S_3		1.00	−0.07	0.01	0.03	−0.07	−0.07	0.10
S_4			1.00	−0.00	−0.00	−0.06	−0.02	−0.01
A_5				1.00	−0.07	−0.00	0.05	0.08
A_FB^{CP}					1.00	0.01	0.05	0.07
S_7						1.00	−0.08	0.01
A_8							1.00	−0.03
A_9								1.00

Correlation matrix for $15.0 < q^2 < 18.9\,\mathrm{GeV}^2/c^4$								
	F_L	S_3	S_4	A_5	A_FB^{CP}	S_7	A_8	A_9
F_L	1.00	0.20	−0.04	−0.03	0.03	0.00	−0.03	−0.10
S_3		1.00	−0.06	0.03	−0.11	−0.08	0.00	0.13
S_4			1.00	−0.13	−0.03	−0.04	0.13	0.06
A_5				1.00	−0.11	0.05	−0.08	0.05
A_FB^{CP}					1.00	0.10	−0.00	−0.03
S_7						1.00	0.03	0.01
A_8							1.00	−0.07
A_9								1.00

LHCb collaboration

R. Aaij[32], A.S.W. Abdelmotteleb[56], C. Abellán Beteta[50], T. Ackernley[60], B. Adeva[46], M. Adinolfi[54], H. Afsharnia[9], C. Agapopoulou[13], C.A. Aidala[86], S. Aiola[25], Z. Ajaltouni[9], S. Akar[65], J. Albrecht[15], F. Alessio[48], M. Alexander[59], A. Alfonso Albero[45], Z. Aliouche[62], G. Alkhazov[38], P. Alvarez Cartelle[55], S. Amato[2], J.L. Amey[54], Y. Amhis[11], L. An[48], L. Anderlini[22], A. Andreianov[38], M. Andreotti[21], F. Archilli[17], A. Artamonov[44], M. Artuso[68], K. Arzymatov[42], E. Aslanides[10], M. Atzeni[50], B. Audurier[12], S. Bachmann[17], M. Bachmayer[49], J.J. Back[56], P. Baladron Rodriguez[46], V. Balagura[12], W. Baldini[21], J. Baptista Leite[1], M. Barbetti[22], R.J. Barlow[62], S. Barsuk[11], W. Barter[61], M. Bartolini[24,h], F. Baryshnikov[83], J.M. Basels[14], S. Bashir[34], G. Bassi[29], B. Batsukh[68], A. Battig[15], A. Bay[49], A. Beck[56], M. Becker[15], F. Bedeschi[29], I. Bediaga[1], A. Beiter[68], V. Belavin[42], S. Belin[27], V. Bellee[50], K. Belous[44], I. Belov[40], I. Belyaev[41], G. Bencivenni[23], E. Ben-Haim[13], A. Berezhnoy[40], R. Bernet[50], D. Berninghoff[17], H.C. Bernstein[68], C. Bertella[48], A. Bertolin[28], C. Betancourt[50], F. Betti[48], Ia. Bezshyiko[50], S. Bhasin[54], J. Bhom[35], L. Bian[73], M.S. Bieker[15], S. Bifani[53], P. Billoir[13], M. Birch[61], F.C.R. Bishop[55], A. Bitadze[62], A. Bizzeti[22,k], M. Bjørn[63], M.P. Blago[48], T. Blake[56], F. Blanc[49], S. Blusk[68], D. Bobulska[59], J.A. Boelhauve[15], O. Boente Garcia[46], T. Boettcher[65], A. Boldyrev[82], A. Bondar[43], N. Bondar[38,48], S. Borghi[62], M. Borisyak[42], M. Borsato[17], J.T. Borsuk[35], S.A. Bouchiba[49], T.J.V. Bowcock[60], A. Boyer[48], C. Bozzi[21], M.J. Bradley[61], S. Braun[66], A. Brea Rodriguez[46], M. Brodski[48], J. Brodzicka[35], A. Brossa Gonzalo[56], D. Brundu[27], A. Buonaura[50], L. Buonincontri[28], A.T. Burke[62], C. Burr[48], A. Bursche[72], A. Butkevich[39], J.S. Butter[32], J. Buytaert[48], W. Byczynski[48], S. Cadeddu[27], H. Cai[73], R. Calabrese[21,f], L. Calefice[15,13], L. Calero Diaz[23], S. Cali[23], R. Calladine[53], M. Calvi[26,j], M. Calvo Gomez[85], P. Camargo Magalhaes[54], P. Campana[23], A.F. Campoverde Quezada[6], S. Capelli[26,j], L. Capriotti[20,d], A. Carbone[20,d], G. Carboni[31], R. Cardinale[24,h], A. Cardini[27], I. Carli[4], P. Carniti[26,j], L. Carus[14], K. Carvalho Akiba[32], A. Casais Vidal[46], G. Casse[60], M. Cattaneo[48], G. Cavallero[48], S. Celani[49], J. Cerasoli[10], D. Cervenkov[63], A.J. Chadwick[60], M.G. Chapman[54], M. Charles[13], Ph. Charpentier[48], G. Chatzikonstantinidis[53], C.A. Chavez Barajas[60], M. Chefdeville[8], C. Chen[3], S. Chen[4], A. Chernov[35], V. Chobanova[46], S. Cholak[49], M. Chrzaszcz[35], A. Chubykin[38], V. Chulikov[38], P. Ciambrone[23], M.F. Cicala[56], X. Cid Vidal[46], G. Ciezarek[48], P.E.L. Clarke[58], M. Clemencic[48], H.V. Cliff[55], J. Closier[48], J.L. Cobbledick[62], V. Coco[48], J.A.B. Coelho[11], J. Cogan[10], E. Cogneras[9], L. Cojocariu[37], P. Collins[48], T. Colombo[48], L. Congedo[19,c], A. Contu[27], N. Cooke[53], G. Coombs[59], I. Corredoira [46], G. Corti[48], C.M. Costa Sobral[56], B. Couturier[48], D.C. Craik[64], J. Crkovská[67], M. Cruz Torres[1], R. Currie[58], C.L. Da Silva[67], S. Dadabaev[83], L. Dai[71], E. Dall'Occo[15], J. Dalseno[46], C. D'Ambrosio[48], A. Danilina[41], P. d'Argent[48], J.E. Davies[62], A. Davis[62], O. De Aguiar Francisco[62], K. De Bruyn[79], S. De Capua[62], M. De Cian[49], J.M. De Miranda[1], L. De Paula[2], M. De Serio[19,c], D. De Simone[50], P. De Simone[23], J.A. de Vries[80], C.T. Dean[67], D. Decamp[8], V. Dedu[10], L. Del Buono[13], B. Delaney[55], H.-P. Dembinski[15], A. Dendek[34], V. Denysenko[50], D. Derkach[82], O. Deschamps[9], F. Desse[11], F. Dettori[27,e], B. Dey[77], A. Di Cicco[23], P. Di Nezza[23], S. Didenko[83], L. Dieste Maronas[46], H. Dijkstra[48], V. Dobishuk[52], C. Dong[3], A.M. Donohoe[18], F. Dordei[27], A.C. dos Reis[1], L. Douglas[59], A. Dovbnya[51], A.G. Downes[8], M.W. Dudek[35], L. Dufour[48], V. Duk[78], P. Durante[48], J.M. Durham[67], D. Dutta[62], A. Dziurda[35], A. Dzyuba[38], S. Easo[57], U. Egede[69], V. Egorychev[41], S. Eidelman[43,v], S. Eisenhardt[58], S. Ek-In[49], L. Eklund[59,w], S. Ely[68], A. Ene[37], E. Epple[67], S. Escher[14], J. Eschle[50], S. Esen[13], T. Evans[48], A. Falabella[20], J. Fan[3], Y. Fan[6], B. Fang[73], S. Farry[60], D. Fazzini[26,j], M. Féo[48], A. Fernandez Prieto[46], A.D. Fernez[66], F. Ferrari[20,d], L. Ferreira Lopes[49], F. Ferreira Rodrigues[2], S. Ferreres Sole[32], M. Ferrillo[50], M. Ferro-Luzzi[48], S. Filippov[39], R.A. Fini[19], M. Fiorini[21,f], M. Firlej[34], K.M. Fischer[63], D.S. Fitzgerald[86], C. Fitzpatrick[62], T. Fiutowski[34], A. Fkiaras[48], F. Fleuret[12],

M. Fontana[13], F. Fontanelli[24,h], R. Forty[48], D. Foulds-Holt[55], V. Franco Lima[60], M. Franco Sevilla[66], M. Frank[48], E. Franzoso[21], G. Frau[17], C. Frei[48], D.A. Friday[59], J. Fu[25], Q. Fuehring[15], E. Gabriel[32], T. Gaintseva[42], A. Gallas Torreira[46], D. Galli[20,d], S. Gambetta[58,48], Y. Gan[3], M. Gandelman[2], P. Gandini[25], Y. Gao[5], M. Garau[27], L.M. Garcia Martin[56], P. Garcia Moreno[45], J. García Pardiñas[26,j], B. Garcia Plana[46], F.A. Garcia Rosales[12], L. Garrido[45], C. Gaspar[48], R.E. Geertsema[32], D. Gerick[17], L.L. Gerken[15], E. Gersabeck[62], M. Gersabeck[62], T. Gershon[56], D. Gerstel[10], Ph. Ghez[8], L. Giambastiani[28], V. Gibson[55], H.K. Giemza[36], A.L. Gilman[63], M. Giovannetti[23,p], A. Gioventù[46], P. Gironella Gironell[45], L. Giubega[37], C. Giugliano[21,f,48], K. Gizdov[58], E.L. Gkougkousis[48], V.V. Gligorov[13], C. Göbel[70], E. Golobardes[85], D. Golubkov[41], A. Golutvin[61,83], A. Gomes[1,a], S. Gomez Fernandez[45], F. Goncalves Abrantes[63], M. Goncerz[35], G. Gong[3], P. Gorbounov[41], I.V. Gorelov[40], C. Gotti[26], E. Govorkova[48], J.P. Grabowski[17], T. Grammatico[13], L.A. Granado Cardoso[48], E. Graugés[45], E. Graverini[49], G. Graziani[22], A. Grecu[37], L.M. Greeven[32], N.A. Grieser[4], L. Grillo[62], S. Gromov[83], B.R. Gruberg Cazon[63], C. Gu[3], M. Guarise[21], P. A. Günther[17], E. Gushchin[39], A. Guth[14], Y. Guz[44], T. Gys[48], T. Hadavizadeh[69], G. Haefeli[49], C. Haen[48], J. Haimberger[48], T. Halewood-leagas[60], P.M. Hamilton[66], J.P. Hammerich[60], Q. Han[7], X. Han[17], T.H. Hancock[63], S. Hansmann-Menzemer[17], N. Harnew[63], T. Harrison[60], C. Hasse[48], M. Hatch[48], J. He[6,b], M. Hecker[61], K. Heijhoff[32], K. Heinicke[15], A.M. Hennequin[48], K. Hennessy[60], L. Henry[48], J. Heuel[14], A. Hicheur[2], D. Hill[49], M. Hilton[62], S.E. Hollitt[15], J. Hu[17], J. Hu[72], W. Hu[7], X. Hu[3], W. Huang[6], X. Huang[73], W. Hulsbergen[32], R.J. Hunter[56], M. Hushchyn[82], D. Hutchcroft[60], D. Hynds[32], P. Ibis[15], M. Idzik[34], D. Ilin[38], P. Ilten[65], A. Inglessi[38], A. Ishteev[83], K. Ivshin[38], R. Jacobsson[48], H. Jage[14], S. Jakobsen[48], E. Jans[32], B.K. Jashal[47], A. Jawahery[66], V. Jevtic[15], F. Jiang[3], M. John[63], D. Johnson[48], C.R. Jones[55], T.P. Jones[56], B. Jost[48], N. Jurik[48], S.H. Kalavan Kadavath[34], S. Kandybei[51], Y. Kang[3], M. Karacson[48], M. Karpov[82], F. Keizer[48], D.M. Keller[68], M. Kenzie[56], T. Ketel[33], B. Khanji[15], A. Kharisova[84], S. Kholodenko[44], T. Kirn[14], V.S. Kirsebom[49], O. Kitouni[64], S. Klaver[32], N. Kleijne[29], K. Klimaszewski[36], M.R. Kmiec[36], S. Koliiev[52], A. Kondybayeva[83], A. Konoplyannikov[41], P. Kopciewicz[34], R. Kopecna[17], P. Koppenburg[32], M. Korolev[40], I. Kostiuk[32,52], O. Kot[52], S. Kotriakhova[21,38], P. Kravchenko[38], L. Kravchuk[39], R.D. Krawczyk[48], M. Kreps[56], F. Kress[61], S. Kretzschmar[14], P. Krokovny[43,v], W. Krupa[34], W. Krzemien[36], W. Kucewicz[35,t], M. Kucharczyk[35], V. Kudryavtsev[43,v], H.S. Kuindersma[32,33], G.J. Kunde[67], T. Kvaratskheliya[41], D. Lacarrere[48], G. Lafferty[62], A. Lai[27], A. Lampis[27], D. Lancierini[50], J.J. Lane[62], R. Lane[54], G. Lanfranchi[23], C. Langenbruch[14], J. Langer[15], O. Lantwin[83], T. Latham[56], F. Lazzari[29,q], R. Le Gac[10], S.H. Lee[86], R. Lefèvre[9], A. Leflat[40], S. Legotin[83], O. Leroy[10], T. Lesiak[35], B. Leverington[17], H. Li[72], P. Li[17], S. Li[7], Y. Li[4], Y. Li[4], Z. Li[68], X. Liang[68], T. Lin[61], R. Lindner[48], V. Lisovskyi[15], R. Litvinov[27], G. Liu[72], H. Liu[6], S. Liu[4], A. Lobo Salvia[45], A. Loi[27], J. Lomba Castro[46], I. Longstaff[59], J.H. Lopes[2], S. Lopez Solino[46], G.H. Lovell[55], Y. Lu[4], C. Lucarelli[22], D. Lucchesi[28,l], S. Luchuk[39], M. Lucio Martinez[32], V. Lukashenko[32,52], Y. Luo[3], A. Lupato[62], E. Luppi[21,f], O. Lupton[56], A. Lusiani[29,m], X. Lyu[6], L. Ma[4], R. Ma[6], S. Maccolini[20,d], F. Machefert[11], F. Maciuc[37], V. Macko[49], P. Mackowiak[15], S. Maddrell-Mander[54], O. Madejczyk[34], L.R. Madhan Mohan[54], O. Maev[38], A. Maevskiy[82], D. Maisuzenko[38], M.W. Majewski[34], J.J. Malczewski[35], S. Malde[63], B. Malecki[48], A. Malinin[81], T. Maltsev[43,v], H. Malygina[17], G. Manca[27,e], G. Mancinelli[10], D. Manuzzi[20,d], D. Marangotto[25,i], J. Maratas[9,s], J.F. Marchand[8], U. Marconi[20], S. Mariani[22,g], C. Marin Benito[48], M. Marinangeli[49], J. Marks[17], A.M. Marshall[54], P.J. Marshall[60], G. Martellotti[30], L. Martinazzoli[48,j], M. Martinelli[26,j], D. Martinez Santos[46], F. Martinez Vidal[47], A. Massafferri[1], M. Materok[14], R. Matev[48], A. Mathad[50], Z. Mathe[48], V. Matiunin[41], C. Matteuzzi[26], K.R. Mattioli[86], A. Mauri[32], E. Maurice[12], J. Mauricio[45], M. Mazurek[48], M. McCann[61], L. Mcconnell[18], T.H. Mcgrath[62], N.T. Mchugh[59], A. McNab[62], R. McNulty[18], J.V. Mead[60], B. Meadows[65], G. Meier[15], N. Meinert[76], D. Melnychuk[36], S. Meloni[26,j], M. Merk[32,80], A. Merli[25], L. Meyer Garcia[2],

M. Mikhasenko[48], D.A. Milanes[74], E. Millard[56], M. Milovanovic[48], M.-N. Minard[8], A. Minotti[26,j], L. Minzoni[21,f], S.E. Mitchell[58], B. Mitreska[62], D.S. Mitzel[48], A. Mödden [15], R.A. Mohammed[63], R.D. Moise[61], T. Mombächer[46], I.A. Monroy[74], S. Monteil[9], M. Morandin[28], G. Morello[23], M.J. Morello[29,m], J. Moron[34], A.B. Morris[75], A.G. Morris[56], R. Mountain[68], H. Mu[3], F. Muheim[58,48], M. Mulder[48], D. Müller[48], K. Müller[50], C.H. Murphy[63], D. Murray[62], P. Muzzetto[27,48], P. Naik[54], T. Nakada[49], R. Nandakumar[57], T. Nanut[49], I. Nasteva[2], M. Needham[58], I. Neri[21], N. Neri[25,i], S. Neubert[75], N. Neufeld[48], R. Newcombe[61], T.D. Nguyen[49], C. Nguyen-Mau[49,x], E.M. Niel[11], S. Nieswand[14], N. Nikitin[40], N.S. Nolte[64], C. Normand[8], C. Nunez[86], A. Oblakowska-Mucha[34], V. Obraztsov[44], T. Oeser[14], D.P. O'Hanlon[54], S. Okamura[21], R. Oldeman[27,e], M.E. Olivares[68], C.J.G. Onderwater[79], R.H. O'neil[58], A. Ossowska[35], J.M. Otalora Goicochea[2], T. Ovsiannikova[41], P. Owen[50], A. Oyanguren[47], K.O. Padeken[75], B. Pagare[56], P.R. Pais[48], T. Pajero[63], A. Palano[19], M. Palutan[23], Y. Pan[62], G. Panshin[84], A. Papanestis[57], M. Pappagallo[19,c], L.L. Pappalardo[21,f], C. Pappenheimer[65], W. Parker[66], C. Parkes[62], B. Passalacqua[21], G. Passaleva[22], A. Pastore[19], M. Patel[61], C. Patrignani[20,d], C.J. Pawley[80], A. Pearce[48], A. Pellegrino[32], M. Pepe Altarelli[48], S. Perazzini[20], D. Pereima[41], A. Pereiro Castro[46], P. Perret[9], M. Petric[59,48], K. Petridis[54], A. Petrolini[24,h], A. Petrov[81], S. Petrucci[58], M. Petruzzo[25], T.T.H. Pham[68], A. Philippov[42], L. Pica[29,m], M. Piccini[78], B. Pietrzyk[8], G. Pietrzyk[49], M. Pili[63], D. Pinci[30], F. Pisani[48], M. Pizzichemi[26,48,j], Resmi P.K[10], V. Placinta[37], J. Plews[53], M. Plo Casasus[46], F. Polci[13], M. Poli Lener[23], M. Poliakova[68], A. Poluektov[10], N. Polukhina[83,u], I. Polyakov[68], E. Polycarpo[2], S. Ponce[48], D. Popov[6,48], S. Popov[42], S. Poslavskii[44], K. Prasanth[35], L. Promberger[48], C. Prouve[46], V. Pugatch[52], V. Puill[11], H. Pullen[63], G. Punzi[29,n], H. Qi[3], W. Qian[6], J. Qin[6], N. Qin[3], R. Quagliani[13], B. Quintana[8], N.V. Raab[18], R.I. Rabadan Trejo[6], B. Rachwal[34], J.H. Rademacker[54], M. Rama[29], M. Ramos Pernas[56], M.S. Rangel[2], F. Ratnikov[42,82], G. Raven[33], M. Reboud[8], F. Redi[49], F. Reiss[62], C. Remon Alepuz[47], Z. Ren[3], V. Renaudin[63], R. Ribatti[29], S. Ricciardi[57], K. Rinnert[60], P. Robbe[11], G. Robertson[58], A.B. Rodrigues[49], E. Rodrigues[60], J.A. Rodriguez Lopez[74], E.R.R. Rodriguez Rodriguez[46], A. Rollings[63], P. Roloff[48], V. Romanovskiy[44], M. Romero Lamas[46], A. Romero Vidal[46], J.D. Roth[86], M. Rotondo[23], M.S. Rudolph[68], T. Ruf[48], R.A. Ruiz Fernandez[46], J. Ruiz Vidal[47], A. Ryzhikov[82], J. Ryzka[34], J.J. Saborido Silva[46], N. Sagidova[38], N. Sahoo[56], B. Saitta[27,e], M. Salomoni[48], C. Sanchez Gras[32], R. Santacesaria[30], C. Santamarina Rios[46], M. Santimaria[23], E. Santovetti[31,p], D. Saranin[83], G. Sarpis[14], M. Sarpis[75], A. Sarti[30], C. Satriano[30,o], A. Satta[31], M. Saur[15], D. Savrina[41,40], H. Sazak[9], L.G. Scantlebury Smead[63], A. Scarabotto[13], S. Schael[14], S. Scherl[60], M. Schiller[59], H. Schindler[48], M. Schmelling[16], B. Schmidt[48], S. Schmitt[14], O. Schneider[49], A. Schopper[48], M. Schubiger[32], S. Schulte[49], M.H. Schune[11], R. Schwemmer[48], B. Sciascia[23], S. Sellam[46], A. Semennikov[41], M. Senghi Soares[33], A. Sergi[24,h], N. Serra[50], L. Sestini[28], A. Seuthe[15], Y. Shang[5], D.M. Shangase[86], M. Shapkin[44], I. Shchemerov[83], L. Shchutska[49], T. Shears[60], L. Shekhtman[43,v], Z. Shen[5], V. Shevchenko[81], E.B. Shields[26,j], Y. Shimizu[11], E. Shmanin[83], J.D. Shupperd[68], B.G. Siddi[21], R. Silva Coutinho[50], G. Simi[28], S. Simone[19,c], N. Skidmore[62], T. Skwarnicki[68], M.W. Slater[53], I. Slazyk[21,f], J.C. Smallwood[63], J.G. Smeaton[55], A. Smetkina[41], E. Smith[50], M. Smith[61], A. Snoch[32], M. Soares[20], L. Soares Lavra[9], M.D. Sokoloff[65], F.J.P. Soler[59], A. Solovev[38], I. Solovyev[38], F.L. Souza De Almeida[2], B. Souza De Paula[2], B. Spaan[15], E. Spadaro Norella[25], P. Spradlin[59], F. Stagni[48], M. Stahl[65], S. Stahl[48], S. Stanislaus[63], O. Steinkamp[50,83], O. Stenyakin[44], H. Stevens[15], S. Stone[68], M.E. Stramaglia[49], M. Straticiuc[37], D. Strekalina[83], F. Suljik[63], J. Sun[27], L. Sun[73], Y. Sun[66], P. Svihra[62], P.N. Swallow[53], K. Swientek[34], A. Szabelski[36], T. Szumlak[34], M. Szymanski[48], S. Taneja[62], A.R. Tanner[54], M.D. Tat[63], A. Terentev[83], F. Teubert[48], E. Thomas[48], D.J.D. Thompson[53], K.A. Thomson[60], V. Tisserand[9], S. T'Jampens[8], M. Tobin[4], L. Tomassetti[21,f], X. Tong[5], D. Torres Machado[1], D.Y. Tou[13], M.T. Tran[49], E. Trifonova[83], C. Trippl[49], G. Tuci[29,n], A. Tully[49], N. Tuning[32,48], A. Ukleja[36],

D.J. Unverzagt[17], E. Ursov[83], A. Usachov[32], A. Ustyuzhanin[42,82], U. Uwer[17], A. Vagner[84], V. Vagnoni[20], A. Valassi[48], G. Valenti[20], N. Valls Canudas[85], M. van Beuzekom[32], M. Van Dijk[49], E. van Herwijnen[83], C.B. Van Hulse[18], M. van Veghel[79], R. Vazquez Gomez[45], P. Vazquez Regueiro[46], C. Vázquez Sierra[48], S. Vecchi[21], J.J. Velthuis[54], M. Veltri[22,r], A. Venkateswaran[68], M. Veronesi[32], M. Vesterinen[56], D. Vieira[65], M. Vieites Diaz[49], H. Viemann[76], X. Vilasis-Cardona[85], E. Vilella Figueras[60], A. Villa[20], P. Vincent[13], F.C. Volle[11], D. Vom Bruch[10], A. Vorobyev[38], V. Vorobyev[43,v], N. Voropaev[38], K. Vos[80], R. Waldi[17], J. Walsh[29], C. Wang[17], J. Wang[5], J. Wang[4], J. Wang[3], J. Wang[73], M. Wang[3], R. Wang[54], Y. Wang[7], Z. Wang[50], Z. Wang[3], Z. Wang[6], J.A. Ward[56], H.M. Wark[60], N.K. Watson[53], S.G. Weber[13], D. Websdale[61], C. Weisser[64], B.D.C. Westhenry[54], D.J. White[62], M. Whitehead[54], A.R. Wiederhold[56], D. Wiedner[15], G. Wilkinson[63], M. Wilkinson[68], I. Williams[55], M. Williams[64], M.R.J. Williams[58], F.F. Wilson[57], W. Wislicki[36], M. Witek[35], L. Witola[17], G. Wormser[11], S.A. Wotton[55], H. Wu[68], K. Wyllie[48], Z. Xiang[6], D. Xiao[7], Y. Xie[7], A. Xu[5], J. Xu[6], L. Xu[3], M. Xu[7], Q. Xu[6], Z. Xu[5], Z. Xu[6], D. Yang[3], S. Yang[6], Y. Yang[6], Z. Yang[5], Z. Yang[66], Y. Yao[68], L.E. Yeomans[60], H. Yin[7], J. Yu[71], X. Yuan[68], O. Yushchenko[44], E. Zaffaroni[49], M. Zavertyaev[16,u], M. Zdybal[35], O. Zenaiev[48], M. Zeng[3], D. Zhang[7], L. Zhang[3], S. Zhang[71], S. Zhang[5], Y. Zhang[5], Y. Zhang[63], A. Zharkova[83], A. Zhelezov[17], Y. Zheng[6], T. Zhou[5], X. Zhou[6], Y. Zhou[6], V. Zhovkovska[11], X. Zhu[3], Z. Zhu[6], V. Zhukov[14,40], J.B. Zonneveld[58], Q. Zou[4], S. Zucchelli[20,d], D. Zuliani[28], G. Zunica[62].

[1] *Centro Brasileiro de Pesquisas Físicas (CBPF), Rio de Janeiro, Brazil*
[2] *Universidade Federal do Rio de Janeiro (UFRJ), Rio de Janeiro, Brazil*
[3] *Center for High Energy Physics, Tsinghua University, Beijing, China*
[4] *Institute Of High Energy Physics (IHEP), Beijing, China*
[5] *School of Physics State Key Laboratory of Nuclear Physics and Technology, Peking University, Beijing, China*
[6] *University of Chinese Academy of Sciences, Beijing, China*
[7] *Institute of Particle Physics, Central China Normal University, Wuhan, Hubei, China*
[8] *Univ. Savoie Mont Blanc, CNRS, IN2P3-LAPP, Annecy, France*
[9] *Université Clermont Auvergne, CNRS/IN2P3, LPC, Clermont-Ferrand, France*
[10] *Aix Marseille Univ, CNRS/IN2P3, CPPM, Marseille, France*
[11] *Université Paris-Saclay, CNRS/IN2P3, IJCLab, Orsay, France*
[12] *Laboratoire Leprince-Ringuet, CNRS/IN2P3, Ecole Polytechnique, Institut Polytechnique de Paris, Palaiseau, France*
[13] *LPNHE, Sorbonne Université, Paris Diderot Sorbonne Paris Cité, CNRS/IN2P3, Paris, France*
[14] *I. Physikalisches Institut, RWTH Aachen University, Aachen, Germany*
[15] *Fakultät Physik, Technische Universität Dortmund, Dortmund, Germany*
[16] *Max-Planck-Institut für Kernphysik (MPIK), Heidelberg, Germany*
[17] *Physikalisches Institut, Ruprecht-Karls-Universität Heidelberg, Heidelberg, Germany*
[18] *School of Physics, University College Dublin, Dublin, Ireland*
[19] *INFN Sezione di Bari, Bari, Italy*
[20] *INFN Sezione di Bologna, Bologna, Italy*
[21] *INFN Sezione di Ferrara, Ferrara, Italy*
[22] *INFN Sezione di Firenze, Firenze, Italy*
[23] *INFN Laboratori Nazionali di Frascati, Frascati, Italy*
[24] *INFN Sezione di Genova, Genova, Italy*
[25] *INFN Sezione di Milano, Milano, Italy*
[26] *INFN Sezione di Milano-Bicocca, Milano, Italy*
[27] *INFN Sezione di Cagliari, Monserrato, Italy*
[28] *Universita degli Studi di Padova, Universita e INFN, Padova, Padova, Italy*
[29] *INFN Sezione di Pisa, Pisa, Italy*
[30] *INFN Sezione di Roma La Sapienza, Roma, Italy*
[31] *INFN Sezione di Roma Tor Vergata, Roma, Italy*
[32] *Nikhef National Institute for Subatomic Physics, Amsterdam, Netherlands*

[33] *Nikhef National Institute for Subatomic Physics and VU University Amsterdam, Amsterdam, Netherlands*
[34] *AGH - University of Science and Technology, Faculty of Physics and Applied Computer Science, Kraków, Poland*
[35] *Henryk Niewodniczanski Institute of Nuclear Physics Polish Academy of Sciences, Kraków, Poland*
[36] *National Center for Nuclear Research (NCBJ), Warsaw, Poland*
[37] *Horia Hulubei National Institute of Physics and Nuclear Engineering, Bucharest-Magurele, Romania*
[38] *Petersburg Nuclear Physics Institute NRC Kurchatov Institute (PNPI NRC KI), Gatchina, Russia*
[39] *Institute for Nuclear Research of the Russian Academy of Sciences (INR RAS), Moscow, Russia*
[40] *Institute of Nuclear Physics, Moscow State University (SINP MSU), Moscow, Russia*
[41] *Institute of Theoretical and Experimental Physics NRC Kurchatov Institute (ITEP NRC KI), Moscow, Russia*
[42] *Yandex School of Data Analysis, Moscow, Russia*
[43] *Budker Institute of Nuclear Physics (SB RAS), Novosibirsk, Russia*
[44] *Institute for High Energy Physics NRC Kurchatov Institute (IHEP NRC KI), Protvino, Russia, Protvino, Russia*
[45] *ICCUB, Universitat de Barcelona, Barcelona, Spain*
[46] *Instituto Galego de Física de Altas Enerxías (IGFAE), Universidade de Santiago de Compostela, Santiago de Compostela, Spain*
[47] *Instituto de Fisica Corpuscular, Centro Mixto Universidad de Valencia - CSIC, Valencia, Spain*
[48] *European Organization for Nuclear Research (CERN), Geneva, Switzerland*
[49] *Institute of Physics, Ecole Polytechnique Fédérale de Lausanne (EPFL), Lausanne, Switzerland*
[50] *Physik-Institut, Universität Zürich, Zürich, Switzerland*
[51] *NSC Kharkiv Institute of Physics and Technology (NSC KIPT), Kharkiv, Ukraine*
[52] *Institute for Nuclear Research of the National Academy of Sciences (KINR), Kyiv, Ukraine*
[53] *University of Birmingham, Birmingham, United Kingdom*
[54] *H.H. Wills Physics Laboratory, University of Bristol, Bristol, United Kingdom*
[55] *Cavendish Laboratory, University of Cambridge, Cambridge, United Kingdom*
[56] *Department of Physics, University of Warwick, Coventry, United Kingdom*
[57] *STFC Rutherford Appleton Laboratory, Didcot, United Kingdom*
[58] *School of Physics and Astronomy, University of Edinburgh, Edinburgh, United Kingdom*
[59] *School of Physics and Astronomy, University of Glasgow, Glasgow, United Kingdom*
[60] *Oliver Lodge Laboratory, University of Liverpool, Liverpool, United Kingdom*
[61] *Imperial College London, London, United Kingdom*
[62] *Department of Physics and Astronomy, University of Manchester, Manchester, United Kingdom*
[63] *Department of Physics, University of Oxford, Oxford, United Kingdom*
[64] *Massachusetts Institute of Technology, Cambridge, MA, United States*
[65] *University of Cincinnati, Cincinnati, OH, United States*
[66] *University of Maryland, College Park, MD, United States*
[67] *Los Alamos National Laboratory (LANL), Los Alamos, United States*
[68] *Syracuse University, Syracuse, NY, United States*
[69] *School of Physics and Astronomy, Monash University, Melbourne, Australia, associated to* [56]
[70] *Pontifícia Universidade Católica do Rio de Janeiro (PUC-Rio), Rio de Janeiro, Brazil, associated to* [2]
[71] *Physics and Micro Electronic College, Hunan University, Changsha City, China, associated to* [7]
[72] *Guangdong Provincial Key Laboratory of Nuclear Science, Guangdong-Hong Kong Joint Laboratory of Quantum Matter, Institute of Quantum Matter, South China Normal University, Guangzhou, China, associated to* [3]
[73] *School of Physics and Technology, Wuhan University, Wuhan, China, associated to* [3]
[74] *Departamento de Fisica , Universidad Nacional de Colombia, Bogota, Colombia, associated to* [13]
[75] *Universität Bonn - Helmholtz-Institut für Strahlen und Kernphysik, Bonn, Germany, associated to* [17]
[76] *Institut für Physik, Universität Rostock, Rostock, Germany, associated to* [17]
[77] *Eotvos Lorand University, Budapest, Hungary, associated to* [48]
[78] *INFN Sezione di Perugia, Perugia, Italy, associated to* [21]
[79] *Van Swinderen Institute, University of Groningen, Groningen, Netherlands, associated to* [32]
[80] *Universiteit Maastricht, Maastricht, Netherlands, associated to* [32]
[81] *National Research Centre Kurchatov Institute, Moscow, Russia, associated to* [41]

[82] National Research University Higher School of Economics, Moscow, Russia, associated to [42]
[83] National University of Science and Technology "MISIS", Moscow, Russia, associated to [41]
[84] National Research Tomsk Polytechnic University, Tomsk, Russia, associated to [41]
[85] DS4DS, La Salle, Universitat Ramon Llull, Barcelona, Spain, associated to [45]
[86] University of Michigan, Ann Arbor, United States, associated to [68]

[a] Universidade Federal do Triângulo Mineiro (UFTM), Uberaba-MG, Brazil
[b] Hangzhou Institute for Advanced Study, UCAS, Hangzhou, China
[c] Università di Bari, Bari, Italy
[d] Università di Bologna, Bologna, Italy
[e] Università di Cagliari, Cagliari, Italy
[f] Università di Ferrara, Ferrara, Italy
[g] Università di Firenze, Firenze, Italy
[h] Università di Genova, Genova, Italy
[i] Università degli Studi di Milano, Milano, Italy
[j] Università di Milano Bicocca, Milano, Italy
[k] Università di Modena e Reggio Emilia, Modena, Italy
[l] Università di Padova, Padova, Italy
[m] Scuola Normale Superiore, Pisa, Italy
[n] Università di Pisa, Pisa, Italy
[o] Università della Basilicata, Potenza, Italy
[p] Università di Roma Tor Vergata, Roma, Italy
[q] Università di Siena, Siena, Italy
[r] Università di Urbino, Urbino, Italy
[s] MSU - Iligan Institute of Technology (MSU-IIT), Iligan, Philippines
[t] AGH - University of Science and Technology, Faculty of Computer Science, Electronics and Telecommunications, Kraków, Poland
[u] P.N. Lebedev Physical Institute, Russian Academy of Science (LPI RAS), Moscow, Russia
[v] Novosibirsk State University, Novosibirsk, Russia
[w] Department of Physics and Astronomy, Uppsala University, Uppsala, Sweden
[x] Hanoi University of Science, Hanoi, Vietnam